This manuscript has been accepted for publication in *Earth and Planetary Science Letters*. Please cite this article as: **Gleeson et al. (2020). Novel insights from Fe-isotopes into the lithological heterogeneity of Ocean Island Basalts and plume-influenced MORBS. *Earth and Planetary Science Letters*.** https://doi.org/10.1016/j.epsl.2020.116114

Novel insights from Fe-isotopes into the lithological heterogeneity of Ocean Island Basalts and plume-influenced MORBs

Matthew L. M. Gleeson[1*], Sally A. Gibson[1], and Helen M. Williams[1]

[1]Department of Earth Sciences, University of Cambridge, Downing Street, Cambridge, UK, CB2 3EQ.

Corresponding author email: mlmg3@cam.ac.uk

ABSTRACT

The extent of lithological heterogeneity in the Earth's convecting mantle is highly debated. Whilst the presence of pyroxenite in the mantle source regions of Ocean Island Basalts (OIBs) has traditionally been constrained using the minor-element chemistry of olivine phenocrysts, recent studies have shown that the Ni and Mn contents of primitive olivines are influenced by the conditions of mantle melting, as well as magma chamber processes. Nevertheless, constraining the lithological properties of the mantle is important due to it's influence on the P-T path followed by solid mantle material during adiabatic ascent, as well as the density of upwelling mantle plumes. We have therefore explored the use of Fe-isotopes as a novel method of tracing lithological heterogeneity in the mantle source regions beneath plume-influenced segments of the global Mid-Ocean Ridge system as well as OIBs.

We present new Fe-isotope ($\delta^{56}Fe$) and trace-element data for 26 basaltic glasses from the plume-influenced Galápagos Spreading Centre to investigate the relative roles of pyroxenite and peridotite in the mantle source region of oceanic basalts. Our data reveals significant heterogeneity in the Fe-isotope composition of the Galápagos Spreading Centre basalts (+0.05 - +0.25‰ $\delta^{56}Fe$), which correlates with key major- and trace-element parameters (e.g. $CaO_{(8)}/Al_2O_{3(8)}$, $[La/Sm]_n$). Application of new models developed to calculate Fe-isotope fractionation during mantle melting, alongside Monte Carlo simulations for melting of a 2-component peridotite mantle, show that this

This manuscript has been accepted for publication in *Earth and Planetary Science Letters*. Please cite this article as: **Gleeson et al. (2020). Novel insights from Fe-isotopes into the lithological heterogeneity of Ocean Island Basalts and plume-influenced MORBS. *Earth and Planetary Science Letters*.** https://doi.org/10.1016/j.epsl.2020.116114

variation cannot be caused by changes in melting processes and/or oxygen fugacity of a peridotitic mantle. Instead, our new δ^{56}Fe data is best explained by variations in the proportion of isotopically-heavy pyroxenite-derived melt that contributes to the GSC basalts, and conclusively shows that lithological heterogeneity exists in the Galápagos mantle plume. Our findings have implications for the moderately-heavy δ^{56}Fe compositions measured in plume-influenced basalts from the Society Islands, Rochambeau Ridges of the Lau back-arc basin, and the FAMOUS segment of the Mid-Atlantic Ridge, which we suggest may also represent contribution from pyroxenite-derived melts.

Keywords: Pyroxenite, Fe-isotopes, Galapagos, Mantle Heterogeneity, MORBs

1 INTRODUCTION

Seismic tomography and distinctive geochemical signatures of Ocean Island Basalts (OIBs) and Mid-Ocean Ridge Basalts (MORBs) provide compelling evidence for recycling of lithospheric components into the convecting mantle, and subsequent incorporation of this material into upwelling mantle plumes (Hofmann, 1997; van der Hilst et al., 1997). Whilst the presence of recycled material in the Earth's mantle, and its lithological properties (i.e. relative modal proportions of olivine and pyroxene), have important implications for mantle dynamics and the density of upwelling mantle plumes (Shorttle et al., 2014), the nature and abundance of these components is poorly constrained.

Incorporation of recycled oceanic lithosphere into the convecting mantle is widely believed to result in the presence of lithologically-distinct components via high-pressure melting of eclogite (metamorphosed remnants of recycled slabs), and subsequent reaction of these melts with surrounding peridotite (Sobolev et al., 2007). This results in the formation of pyroxene-rich (and highly fusible) components in the mantle (pyroxenite; Sobolev et al., 2007; Yaxley and Green, 1998). Identification of this lithologically-distinct material in the mantle source region of OIBs and MORBs has classically been achieved using minor-element concentrations in olivine (Herzberg, 2011; Sobolev

This manuscript has been accepted for publication in *Earth and Planetary Science Letters*. Please cite this article as: **Gleeson et al. (2020). Novel insights from Fe-isotopes into the lithological heterogeneity of Ocean Island Basalts and plume-influenced MORBS. *Earth and Planetary Science Letters*.** https://doi.org/10.1016/j.epsl.2020.116114

et al., 2007), major-element compositions of high MgO basalts (Lambart et al., 2013), and ratios of first row transition elements (Davis et al., 2013). However, these methods are subject to considerable uncertainties regarding: (i) the influence of temperature, pressure, and oxygen fugacity (fO_2) during mantle melting (Matzen et al., 2017b); and (ii) the influence that crustal processes may play (Gleeson and Gibson, 2019). In particular, it is still uncertain whether Ca, Ni, and Mn concentrations in magmatic olivines can be used, unambiguously, to distinguish between peridotite and pyroxenite derived melts and it is therefore important to develop additional tracers for pyroxenite melting (Gleeson and Gibson, 2019; Matzen et al., 2017b, 2017a; Putirka et al., 2011; Rhodes et al., 2012).

Here we investigate the use of stable Fe-isotopes ($\delta^{56}Fe$) as an alternative method for identifying lithological heterogeneity in the mantle source region of oceanic basalts (Konter et al., 2016; Nebel et al., 2019; Williams and Bizimis, 2014). As Fe is stoichiometrically incorporated into mantle minerals, variations in $\delta^{56}Fe$ likely represent changes in the mass fraction contribution from different mantle components. Therefore, variations in $\delta^{56}Fe$ have the potential to provide a very different perspective on mantle heterogeneity compared to traditional radiogenic isotope ratios (e.g. Sr, Pb) that tend to be dominated by relatively small contributions from enriched mantle components and yield little information on mantle lithology.

Traditional stable isotope theory predicts that the extent of isotopic fractionation (i.e. $\Delta^{56}Fe_{A\text{-}B}=\delta^{56}Fe_A-\delta^{56}Fe_B$; where $\delta^{56}Fe$ represents the deviation in $^{56}Fe/^{54}Fe$ from the IRMM-014 standard in parts–per-thousand) is inversely proportional to temperature (i.e. $1/T^2$). Despite the high temperature of igneous processes, recent advances have revealed that magmatic processes (e.g. mantle melting/crystal fractionation) can cause both kinetic and equilibrium stable-isotope fractionation in these systems (Dauphas et al., 2014; Huang et al., 2010; Schuessler et al., 2009; Sossi and O'Neill, 2017; Teng et al., 2011, 2008; Weyer and Ionov, 2007; Zhao et al., 2017). In particular, Fe-isotopes possess relatively large and predictable equilibrium fractionation factors between different minerals and/or melts at magmatic temperatures, due to the polyvalent nature of Fe, as well as variations in the coordination

This manuscript has been accepted for publication in *Earth and Planetary Science Letters*. Please cite this article as: **Gleeson et al. (2020). Novel insights from Fe-isotopes into the lithological heterogeneity of Ocean Island Basalts and plume-influenced MORBS. *Earth and Planetary Science Letters*.** https://doi.org/10.1016/j.epsl.2020.116114

state of Fe in different mineral phases (Sossi and O'Neill, 2017). As heavy Fe-isotopes (e.g. ^{56}Fe, ^{57}Fe) should be preferentially partitioned into the phase with the strongest Fe-O bonds, minerals that incorporate small amounts of Fe^{3+} (e.g. pyroxene) are predicted to have heavier $\delta^{56}Fe$ compositions than those that are deficient in Fe^{3+} (e.g. olivine; Sossi and O'Neill, 2017). This is because the smaller ionic radii and higher valence state of Fe^{3+} results in shorter, and hence stronger, Fe-O bonds (Dauphas et al., 2014).

Due to the non-modal nature of melting in the convecting mantle (i.e. disproportionately high contribution from isotopically-heavy clinopyroxene to the melt phase), and the incompatible nature of Fe^{3+}, primary mantle melts are predicted to be isotopically heavy compared to their mantle source (Dauphas et al., 2009; Williams and Bizimis, 2014). The extent of the Fe-isotope fractionation is also believed to be sensitive to the fO_2 of the mantle, which has previously been used to explain the offset between the average $\delta^{56}Fe$ composition of the terrestrial mantle ($\delta^{56}Fe$=+0.025±0.025‰; based on analyses of abyssal peridotites; Craddock et al., 2013) and MORBs ($\delta^{56}Fe$~+0.1‰; Sossi et al., 2016; Teng et al., 2013). Alternatively, some studies have suggested that the extent of isotopic fractionation during mantle melting may be sensitive to the lithological properties of the source (Sossi and O'Neill, 2017; Williams and Bizimis, 2014). This is due to the greater isotopic fractionation during melting of pyroxene-rich mantle rather than peridotite (Williams and Bizimis, 2014), and the heavy $\delta^{56}Fe$ of pyroxenitic components regardless of formation mechanism (Konter et al., 2016; Nebel et al., 2019; Williams and Bizimis, 2014).

Our study is primarily focused on the Fe-isotope composition of basalts erupted at regularly-spaced intervals on segments of the Galápagos Spreading Centre (GSC) that are influenced by the nearby Galápagos mantle plume (Schilling et al., 2003). These samples exhibit considerable variability in their incompatible trace-element compositions and Sr, Nd and Pb isotope ratios, and range from compositions more depleted than average MORBs to highly enriched basalts (Gibson and Richards,

This manuscript has been accepted for publication in *Earth and Planetary Science Letters*. Please cite this article as: **Gleeson et al. (2020). Novel insights from Fe-isotopes into the lithological heterogeneity of Ocean Island Basalts and plume-influenced MORBS. *Earth and Planetary Science Letters*.** https://doi.org/10.1016/j.epsl.2020.116114

2018; Schilling et al., 2003). If lithological heterogeneity exists in the mantle source region beneath the GSC then it is highly likely to be expressed in the δ^{56}Fe composition of these samples.

2 GEOLOGICAL BACKGROUND

The Galápagos Archipelago (eastern equatorial Pacific) represents one of the most volcanically active regions in the world. The broad geographic distribution of Holocene volcanism in the Galápagos has allowed multiple geochemical studies to place constraints on the spatial heterogeneity of radiogenic isotope ratios in the Galápagos mantle plume (Harpp and White, 2001; White et al., 1993). Analyses of basaltic lavas from across the Galápagos Archipelago reveal the presence of at least 3 isotopically-enriched mantle components that form a horseshoe shape around an isotopically-depleted eastern component (DGM; Fig. 1; Harpp and White, 2001; Hoernle et al., 2000; White et al., 1993).

The 'Western' (PLUME) Galápagos plume component is characterised by high $^{3}He/^{4}He$ ratios and moderately radiogenic Sr and Pb-isotope values (similar to the common plume component referred to as 'FOZO' or 'C'; Hart et al., 1992) and is believed to contain a significant contribution from the primordial mantle (Kurz and Geist, 1999). The 'Southern' (FLO) component is characterised by the most radiogenic Sr and Pb-isotope ratios in the Galápagos. The Pb-isotope signature of the FLO plume component is similar to the global HIMU end-member, although the presence of an EM-type component is required to explain the $^{87}Sr/^{86}Sr$ signatures from this region (Harpp et al., 2014). Recent studies have suggested that this component may represent recycled oceanic crust (Harpp et al., 2014), although olivine chemistry is inconsistent with the presence of a lithologically-distinct pyroxenite (Vidito et al., 2013). The 'Northern' (Wolf-Darwin; WD) Galápagos plume component is characterised by elevated $^{208}Pb/^{206}Pb$ and $^{207}Pb/^{206}Pb$ ratios. Less is known about the origin of this component than the FLO and PLUME components (Harpp and White, 2001).

This manuscript has been accepted for publication in *Earth and Planetary Science Letters*. Please cite this article as: **Gleeson et al. (2020). Novel insights from Fe-isotopes into the lithological heterogeneity of Ocean Island Basalts and plume-influenced MORBS. *Earth and Planetary Science Letters*.** https://doi.org/10.1016/j.epsl.2020.116114

The isotopic heterogeneity observed in plume-derived basalts from across the Galápagos Archipelago is evident in the composition of basalts (D-, N-, and E-MORBs) erupted along the nearest section of the GSC (Gibson et al., 2015), ~150-250 km north of the centre of plume upwelling (Fig. 2). The geochemical heterogeneity displayed by these GSC basalts coincide with variations in geophysical parameters along the GSC (e.g. crustal thickness, bouguer gravity anomalies; Ingle et al., 2010; Mittelstaedt et al., 2014; Schilling et al., 2003). These signatures are thought to result from the transfer of compositionally, and thermally, distinct material from the off-axis Galápagos plume.

Several studies have hypothesised that the geochemical variations displayed by the GSC basalts result from incorporation and mixing of melts from three isotopically distinct components (Gibson et al., 2015; Ingle et al., 2010; Schilling et al., 2003). A sharp change in Ba/Nb, $^{3}He/^{4}He$ and $\Delta^{208}Pb$ across the Galápagos Transform Fault (GTF) at 91°W reveals the incorporation of the WD Galápagos plume component in the shallow mantle beneath the western GSC (but not beneath the eastern GSC; Gibson et al., 2015). In addition, E-MORBs found within ~200 km of the Galápagos Transform Fault contain a significant contribution from low-fraction melts of an isotopically-enriched component in the Galápagos plume (Gibson and Richards, 2018; Ingle et al., 2010). However, the radiogenic isotope composition of this component is debated with some authors suggesting FOZO or C-like compositions (Ingle et al., 2010), whereas others have suggested that this component is similar to the global HIMU endmember (Gibson et al., 2015; Schilling et al., 2003).

We use our new Fe-isotope data from the GSC to evaluate whether any of previously identified components in the Galápagos mantle plume, defined on the basis of Sr, Nd and Pb isotopic ratios (Hoernle et al., 2000; Harpp and White, 2001), are associated with a lithologically-distinct mantle source. This is achieved by integrating 2-component mantle melting models with theoretical predictions of Fe isotope fractionation to constrain the Pb-isotope composition of the isotopically-enriched pyroxenite component that is common to basalts erupted on both the western and eastern

This manuscript has been accepted for publication in *Earth and Planetary Science Letters*. Please cite this article as: **Gleeson et al. (2020). Novel insights from Fe-isotopes into the lithological heterogeneity of Ocean Island Basalts and plume-influenced MORBS. *Earth and Planetary Science Letters*.** https://doi.org/10.1016/j.epsl.2020.116114

GSC. This allows us to place new constraints on the extent and location of lithological heterogeneity in the Galápagos mantle plume.

3 SAMPLES

Twenty-six basaltic glasses from 83°W-98°W on the Galápagos Spreading Centre (GSC) were selected from the J. G. Schilling collection at the University of Rhode Island and analysed for Fe-isotopes. Most of these samples have a geographical spacing of ~30-40 km and span the entire range of incompatible trace-element and radiogenic isotope compositions displayed by GSC basalts (Schilling et al., 2003).

To ensure that our Fe-isotope data represents the composition of GSC basaltic melts that are unaffected by alteration or crystal accumulation (McCoy-West et al., 2018), chips of basaltic glass (approximately 5mm diameter) with no visible signs of alteration/oxidation or notable phenocrysts were hand-picked using a binocular microscope. Backscatter Electron imaging of these samples confirmed that the proportion of olivine and clinopyroxene in each sample was extremely low (<1%).

4 ANALYTICAL METHODS

Prior to Fe-isotope analysis, we analysed the major- and minor-element concentrations of characteristic glass chips from each sample using a Cameca SX100 EPMA in the Department of Earth Sciences at the University of Cambridge. Analysis was carried out using a beam current of 10 nA, an accelerating volatile of 15kV, and a defocused beam (10 μm). Peak count times of 10s were used for Na and K (which were analysed first), and 20s for Ca, Si, Mg, Al, and Fe. Minor elements were analysed for 60s (P, Ti, Cr and Mn). Background counts were collected either side of the peak for half the peak count times. Data quality was checked using three secondary glass standards (two basaltic – including VG-2, one rhyolitic; see Appendix A). Measured compositions are consistently within 1 standard

This manuscript has been accepted for publication in *Earth and Planetary Science Letters*. Please cite this article as: **Gleeson et al. (2020). Novel insights from Fe-isotopes into the lithological heterogeneity of Ocean Island Basalts and plume-influenced MORBS. *Earth and Planetary Science Letters*.** https://doi.org/10.1016/j.epsl.2020.116114

deviation of the preferred values and a precision of <3% was regularly achieved for all major elements except Na (<4%).

Trace-element concentrations were acquired using a 193ESI Laser Ablation system coupled to a Nexion Perkin Elmer ICP-MS in the Department of Earth Sciences, University of Cambridge. Following systematic testing of laser ablation analysis of volcanic glass over a range of spot sizes, fluence and repetition rates, we selected a spot size of 100 μm, fluence of 8 J/cm^2 and repetition rate of 10 Hz for our analysis. Data was only collected from regions of clean, microlite-free, glass so that our analyses were not influenced by accidental ablation of plagioclase microlites. Data reduction was performed using Glitter software©, and then later re-processed in Iolite© with no significant difference observed in the calculated values. ^{29}Si was used as an internal standard, and NIST SRM612 as a primary standard. Repeated measurements of BHVO-2g and BIR-1g secondary standards reveal that a precision of <5% was achieved for most trace elements, and most first-row transition elements (FRTEs). Slightly larger errors (precision of <10%) are seen for the HREE which are only present in low concentrations. Repeated analyses of secondary standards are regularly within 95% and 105% of published values for all elements reported.

Once appropriate chips of each sample of basaltic glass had been chosen, sample dissolution, iron purification and isotopic analyses were carried out in the Department of Earth Sciences, University of Cambridge. Isotopic analyses were performed on a Thermo Neptune multiple-collector inductively coupled plasma mass spectrometer. Sample solutions consisted of ~8.6 ppm Fe in 0.1 M HNO_3. Instrumental mass bias was corrected for by sample standard bracketing, where the sample and standard Fe beam intensities were matched to within 10%. Mass dependence and reproducibility were evaluated using an in-house 'iron chloride' salt standard (δ^{56}Fe = -0.70±0.05‰; δ^{57}Fe = -1.08±0.07‰) that has been analysed in previous studies (Williams and Bizimis, 2014). Chemistry blanks possessed neglible amounts of Fe compared to our samples (<5 ng). The analytical precision

This manuscript has been accepted for publication in *Earth and Planetary Science Letters*. Please cite this article as: **Gleeson et al. (2020). Novel insights from Fe-isotopes into the lithological heterogeneity of Ocean Island Basalts and plume-influenced MORBS. *Earth and Planetary Science Letters*.** https://doi.org/10.1016/j.epsl.2020.116114

of our Fe-isotope analyses is based on between 6 and 12 repeat measurements for each sample and is generally found to be better than ±0.025‰ (2σ for $\delta^{56}Fe$; Table 1). The accuracy of the Fe-isotope analysis was monitored using the USGS BIR-1 secondary standard ($\delta^{56}Fe$= +0.056±0.031‰ (2σ); $\delta^{57}Fe$= +0.081±0.048‰ (2σ); n=9) and was found to be consistent with previous studies (Dauphas et al., 2009; Williams and Bizimis, 2014).

5 RESULTS

We use primitive mantle normalised $[La/Sm]_n$ ratios to define three geochemical types of basalts: E-MORBs ($[La/Sm]_n>1.2$); N-MORBs ($0.8<[La/Sm]_n<1.2$); and D-MORBs ($[La/Sm]_n<0.8$). The N-MORB – E-MORB transition is lower than that suggested by Gale et al. (2014) due to the overall depleted nature of basalts from the Galápagos Spreading Centre. E-MORBs are generally found in the region of greatest plume-influence (between 89.5°W and 92.6°W; Christie et al., 2005; Cushman et al., 2004; Detrick et al., 2002; Gibson et al., 2015; Ingle et al., 2010). In addition, several of the samples that have been analysed from the GSC possess anomalously enriched trace-element compositions ($[Sm/Yb]_n>1.5$). This is believed to represent short-length scale heterogeneity in the delivery of enriched material to the GSC (Gibson and Richards, 2018) .

Clear differences are also seen in the major-element systematics of D-MORBs, N-MORBs, and E-MORBs from the GSC. These relate to variations in the depth of mantle melting (e.g. lower SiO_2 in E-MORBs; Lee et al., 2009) as well as variations in the source properties and/or initial water contents of these magmas (e.g. lower FeO_t and CaO/Al_2O_3 in E-MORBs; Appendix A). These differences indicate that E-MORBs contain contributions of high-pressure (i.e. garnet stability field), H_2O-rich mantle melts (Gibson et al., 2015; Ingle et al., 2010).

The Fe-isotope compositions ($\delta^{56}Fe$) of plume-influenced basalts from between 95.5°W and 85.5°W on the GSC vary from $\delta^{56}Fe$=+0.052‰ to $\delta^{56}Fe$=+0.145‰, with two outliers at $\delta^{56}Fe$=+0.216‰ and

This manuscript has been accepted for publication in *Earth and Planetary Science Letters*. Please cite this article as: **Gleeson et al. (2020). Novel insights from Fe-isotopes into the lithological heterogeneity of Ocean Island Basalts and plume-influenced MORBS. *Earth and Planetary Science Letters*.** https://doi.org/10.1016/j.epsl.2020.116114

δ^{56}Fe=+0.242‰. These two basalts with anomalously heavy δ^{56}Fe are from 90.95°W (TR164 26D-3g) and 86.3°W (ST7-17D-1g) and are distinguished by the fact that they possess the most enriched trace-element signatures (e.g. $[La/Sm]_n$) of any basalt measured along the GSC. In addition, the δ^{56}Fe composition of the remaining samples are shown to generally increase in regions of the GSC where radiogenic isotopes and trace-element ratios provide evidence for a greater contribution from enriched plume material (89.5°W-92.5°W; Gibson and Richards, 2018; Ingle et al., 2010), revealing a systematic relationship between the δ^{56}Fe composition of the GSC basalts and delivery of enriched plume material to the spreading ridge.

Our data reveals that D-MORBs and many N-MORBs from the GSC possess δ^{56}Fe signatures that lie at or below the lower end of those previously measured in MORBs (0.07‰ to +0.14‰; Teng et al., 2013). In addition, no clear difference is observed in the Fe-isotope composition of basalts from the eastern and western GSC (although the lowest values are observed in D-MORBs from the eastern GSC). This indicates that either: (i) there is no difference in the lithological properties/Fe-isotope composition of the depleted Eastern (DGM) and enriched WD plume components; or (ii) the relative fraction of Fe sourced from the WD component along the western GSC is small.

The δ^{56}Fe compositions measured in the GSC basalts show strong correlations with major element parameters (Na_8 and Ca_8/Al_8; fractionation corrected to 8 wt% MgO), and even stronger correlations with incompatible trace-element ratios indicative of both source enrichment and melting processes (e.g. $[Ce/Yb]_n$; $[Sm/Yb]_n$; Fig. 3). No obvious relationship between δ^{56}Fe and radiogenic isotope ratios (e.g. $^{206}Pb/^{204}Pb$) are observed, which, can be explained by mixing relationships where the difference in concentration of Pb (or Sr; Nd and Hf) in melts derived from the enriched and depleted mantle components are large (e.g. $[Pb]_{Enr}/[Pb]_{Dep}$=10-100; Fig. 3). Whilst melts of pyroxenite and/or eclogite components may possess FeO concentrations that are significantly different than melts of a peridotite (Lambart et al., 2013), these differences are unlikely to be as large as those predicted for incompatible

This manuscript has been accepted for publication in *Earth and Planetary Science Letters*. Please cite this article as: **Gleeson et al. (2020). Novel insights from Fe-isotopes into the lithological heterogeneity of Ocean Island Basalts and plume-influenced MORBS. *Earth and Planetary Science Letters*.** https://doi.org/10.1016/j.epsl.2020.116114

trace-elements such as Pb or Sr. As a result, mixing curves between an enriched and depleted melt composition are highly curved, re-creating the observed values in the GSC basalts (Fig. 3d).

6 DISCUSSION

The heterogeneity observed in the δ^{56}Fe composition of the GSC basalts may indicate that there is substantial variability in the lithological properties of the mantle source beneath the GSC. However, to constrain this further it is necessary to evaluate the influence that variations in mantle melting, crystallisation processes, and/or fO_2 may have on the δ^{56}Fe composition of the GSC basalts.

6.1 FRACTIONAL CRYSTALLISATION

Several studies have investigated the influence of crystal fractionation on the δ^{56}Fe of basaltic magmas, but conflicting results indicate that the exact influence of magmatic differentiation is difficult to constrain and may vary between different tectonic settings (McCoy-West et al., 2018; Schuessler et al., 2009; Sossi et al., 2012; Teng et al., 2008). In general, it is assumed that isotopically-light Fe is fractionated into olivine and pyroxene (McCoy-West et al., 2018; Sossi et al., 2012; Teng et al., 2013). This fractionation is driven by the high Fe^{3+} content of basaltic melts compared to these mineral phases as several studies have shown that little to no fractionation of Fe-isotopes occur between olivine and highly reduced basalts that contain no Fe^{3+} (Dauphas et al., 2014; Prissel et al., 2018). In addition, the extent of Fe-isotope fractionation is highly dependent on whether: (i) the system is open or closed to oxygen exchange (Sossi et al., 2012); (ii) isotopic fractionation is controlled by equilibrium and/or kinetic processes (McCoy-West et al., 2018); and (iii) chromite fractionates alongside olivine and hence sequesters isotopically-heavy Fe from the melt phase (McCoy-West et al., 2018).

As the GSC basalts that we have analysed have a narrow range of MgO (~5.5 – 8.5 wt%), the influence of crystal fractionation on δ^{56}Fe is minimised and we have avoided any complications caused by the

This manuscript has been accepted for publication in *Earth and Planetary Science Letters*. Please cite this article as: **Gleeson et al. (2020). Novel insights from Fe-isotopes into the lithological heterogeneity of Ocean Island Basalts and plume-influenced MORBS. *Earth and Planetary Science Letters*.** https://doi.org/10.1016/j.epsl.2020.116114

fractionation of isotopically-heavy magnetite in more evolved magmas (<5 wt% MgO; Sossi et al., 2012). Nevertheless, to ensure that our results are not influenced by variations in magmatic differentiation (E-MORBs tend to possess lower MgO contents than D-MORBs) we have corrected the Fe-isotope, major- and trace-element composition of our samples to 8 wt% MgO using published mineral-melt trace-element partition coefficients and isotope fractionation factors (Sossi et al., 2016; full details can be found in Appendix A).

Due to the considerable uncertainties regarding the influence of crystallisation on the Fe-isotope composition of basaltic lavas, other fractionation factors between olivine/pyroxene and the melt phase were tested to ensure that our results are independent of our fractional crystallisation correction (e.g. from Dauphas et al., 2014; Appendix A). In addition, by applying a correction to 8 wt% MgO, within the range displayed by the GSC basalts, rather than Mg#~70 (i.e. in equilibrium with mantle peridotite), which would require significant extrapolation, we minimise the propagated error that results from this correction.

Our fractionation-corrected dataset displays considerable δ^{56}Fe heterogeneity and confirms that magmatic differentiation does not have a major influence on the variation observed in the δ^{56}Fe composition of the GSC basalts. This demonstrates that significant heterogeneity in the composition of primary mantle melts beneath the GSC must exist. Below we consider whether this variability is related to melting processes (e.g. melt fraction, presence of garnet), or due to heterogeneity in the mantle source (oxidised/lithologically distinct components).

6.2 Melt Fraction and fO_2

As outlined above, heavy Fe isotopes (i.e. ^{56}Fe and ^{57}Fe) are expected to be preferentially partitioned into Fe^{3+} bearing phases (e.g. basaltic melt). As a result, primary mantle melts should possess heavier δ^{56}Fe signatures than their source regions (Dauphas et al., 2014). In theory, this effect should be greatest for early-formed, low-fraction melts that (due to the incompatible nature of Fe^{3+}) are

This manuscript has been accepted for publication in *Earth and Planetary Science Letters*. Please cite this article as: **Gleeson et al. (2020). Novel insights from Fe-isotopes into the lithological heterogeneity of Ocean Island Basalts and plume-influenced MORBS. *Earth and Planetary Science Letters*.** https://doi.org/10.1016/j.epsl.2020.116114

predicted to possess a higher proportion of Fe^{3+} than high-fraction melts (Dauphas et al., 2014, 2009). In addition, an increase in the fO_2 of the source (and therefore an increase in the Fe^{3+} available to enter the melt phase) is predicted to result in a larger fractionation of Fe-isotopes during mantle melting (Dauphas et al., 2014, 2009).

However, there is no clear relationship between Fe^{3+}/Fe_{tot} and indices of melt fraction (e.g. Na_8) for the global MORB dataset (Cottrell and Kelley, 2011) and recent experimental work has shown that the Fe^{3+}/Fe_{tot} of peridotite partial melts remains approximately constant during partial melting (Sorbadere et al., 2018). Nevertheless, it is constructive to consider the maximum Fe-isotope composition that may be produced by low-fraction melting of a highly-oxidised source (~QFM+2), and whether or not these hypothetical melts may explain the composition of the GSC basalts.

To test this hypothesis, we present a new model to calculate the influence of fO_2 on the $\delta^{56}Fe$ composition of mantle melts. Our model uses NRIXS (Nuclear Resonant Inelastic X-ray Scattering) measurements of basaltic glass to quantify the influence of Fe^{3+}/Fe_{tot} on the melt Fe-O force constant (Dauphas et al., 2014), which is used alongside theoretical constraints on the Fe-O force constant for all Fe-bearing mantle minerals (Sossi and O'Neill, 2017) to calculate the $\delta^{56}Fe$ composition of melts formed during melting of mantle peridotite (see Appendix A for details). The results of this analysis indicate that the $\delta^{56}Fe$ composition of melts characterised by very high Fe^{3+}/Fe_{tot} ratios (~0.25) are only ~+0.02‰ $\delta^{56}Fe$ heavier than the $\delta^{56}Fe$ composition of relatively reduced melts (Fe^{3+}/Fe_{tot}=0.13; Fig. 4). Therefore, although the early model of Dauphas et al. (2009) indicates that highly oxidised melts may have a $\delta^{56}Fe$ composition as high as ~+0.18‰ (Konter et al., 2016), we consider it unlikely that variations in fO_2 can explain the heterogeneity observed in the $\delta^{56}Fe$ composition of the GSC basalts.

In addition, none of the basalts from the GSC represent melts of the enriched mantle component alone. Therefore, the $\delta^{56}Fe$ composition of the enriched (and presumably oxidised) melt that is

This manuscript has been accepted for publication in *Earth and Planetary Science Letters*. Please cite this article as: **Gleeson et al. (2020). Novel insights from Fe-isotopes into the lithological heterogeneity of Ocean Island Basalts and plume-influenced MORBS. *Earth and Planetary Science Letters*.** https://doi.org/10.1016/j.epsl.2020.116114

307 required to explain the GSC data is far heavier than that measured in the enriched GSC basalts. To
308 estimate the δ^{56}Fe composition of melts from the enriched mantle component that would be required
309 to explain the δ^{56}Fe heterogeneity of the GSC basalts we estimated the proportion of melt from this
310 component that is needed to explain the incompatible trace-element composition of each basalt. This
311 is done using: (i) a 2-component mantle melting model combined with; (ii) a Markov Chain Monte
312 Carlo (MCMC) algorithm that evaluates and compares the melt composition predicted by each model
313 and the measured REE composition of each GSC basalt (Fig. 5; see Appendix A for details). In all models
314 shown in this study we assume that the primary control on the incompatible trace-element
315 composition of the GSC basalts is the relative velocity of active upwelling below the anhydrous
316 peridotite solidus, consistent with previous studies (e.g. Ingle et al., 2010; Appendix A).

317 The proportion of enriched melt generated in each model, as well as the proportion of melt that is
318 derived from the garnet stability-field, is recorded alongside the deviation between the trace-element
319 composition predicted by each model and the REE composition of each sample. These results are used
320 to generate a probability distribution for the proportion of melt from the enriched mantle component
321 that contributes to the formation of each sample along the GSC (Fig. 5; Appendix A) and reveal a strong
322 correlation between δ^{56}Fe and the mass fraction contribution of enriched melt (Fig. 6a). Using this
323 correlation, we can estimate the δ^{56}Fe composition of melts from the enriched mantle component
324 that would be required to recreate the GSC data. This analysis is carried out for 3 separate scenarios,
325 where melts of the enriched mantle component have FeO concentrations that are: (i) equivalent to
326 (δ^{56}Fe=+0.445±0.050‰); (ii) 1.5 times greater than (δ^{56}Fe=+0.355±0.038‰); and (iii) 2 times greater
327 than (δ^{56}Fe=+0.309±0.033‰) the FeO concentration of melts from the depleted mantle component
328 (Fig. 6a). The results clearly demonstrate that in all scenarios these end-member melt compositions
329 cannot be recreated by any reasonable model of Fe-isotope fractionation during mantle melting of a
330 peridotite mantle (e.g. Dauphas et al., 2009). Therefore, even though the moderately enriched basalts
331 from the GSC have similar δ^{56}Fe compositions to that predicted by the model of Dauphas et al. (2009),

This manuscript has been accepted for publication in *Earth and Planetary Science Letters*. Please cite this article as: **Gleeson et al. (2020). Novel insights from Fe-isotopes into the lithological heterogeneity of Ocean Island Basalts and plume-influenced MORBS. *Earth and Planetary Science Letters*.** https://doi.org/10.1016/j.epsl.2020.116114

variations in melt fraction and/or fO_2 cannot explain the $\delta^{56}Fe$ heterogeneity observed in the GSC basalts.

6.3 INFLUENCE OF ISOTOPICALLY-LIGHT GARNET

Data from both natural samples (Williams et al., 2009), and experimental studies (Sossi and O'Neill, 2017), have shown that garnet preferentially incorporates isotopically-light Fe-isotopes compared to other mantle minerals. It has therefore been hypothesised that primary mantle melts derived from the garnet-stability field may possess heavy Fe-isotope compositions compared to melts from the spinel-stability field (due to the retention of light Fe-isotopes in residual garnet; Nebel et al., 2018; Sossi and O'Neill, 2017). This is an attractive explanation for the heterogeneity observed in the GSC basalts, due to the very strong correlation observed between $\delta^{56}Fe$ and $[Sm/Yb]_n$ (Fig. 3), as well as the strong correlation between $\delta^{56}Fe$ and the proportion of melt derived from the garnet-stability field that is estimated by our MCMC models (Fig. 6b).

However, using theoretical constraints on the garnet-olivine fractionation factors (Sossi and O'Neill, 2017), and our new models of Fe-isotope fractionation during mantle melting, we show that the heaviest $\delta^{56}Fe$ signature that results from small amounts of partial melting of a garnet lherzolite with $\delta^{56}Fe$=+0.025‰ is ~+0.075 - +0.095‰, depending on the Fe^{3+}/Fe_{tot} content of the resulting melt (Fig. 4). This estimate is significantly lighter than a significant number (~6-7) of the E-MORBs from the GSC, and much lighter than the extremely heavy $\delta^{56}Fe$ value of melts from the garnet stability-field that are required to match the data from the GSC ($\delta^{56}Fe$=+0.439±0.053‰ for $[Fe]_{deep}/[Fe]_{shallow}$=1, and $\delta^{56}Fe$=+0.304±0.036‰ for $[Fe]_{deep}/[Fe]_{shallow}$=2; Fig. 6b). As such, the correlation between $\delta^{56}Fe$ and $[Sm/Yb]_n$ does not indicate a causative link between the presence of garnet in a lherzolitic mantle residue and the $\delta^{56}Fe$ composition of the GSC basalts. Therefore, significant lithological heterogeneity and/or heterogeneity in the source $\delta^{56}Fe$ composition must exist to explain the large range observed in the Fe-isotope composition of the GSC basalts.

This manuscript has been accepted for publication in *Earth and Planetary Science Letters*. Please cite this article as: **Gleeson et al. (2020). Novel insights from Fe-isotopes into the lithological heterogeneity of Ocean Island Basalts and plume-influenced MORBS. *Earth and Planetary Science Letters*.** https://doi.org/10.1016/j.epsl.2020.116114

6.4 Fe-isotope Heterogeneity of a metasomatised peridotite

Before we can consider the possibility that the δ^{56}Fe heterogeneity displayed by the GSC basalts is caused by variations in the contribution of melts from a pyroxenitic lithology, we need to evaluate whether these compositions could result incorporation of melts from an isotopically heavy peridotite component. To do so, we take the heaviest δ^{56}Fe value measured in a metasomatized peridotite from Weyer and Ionov (2007; δ^{56}Fe=+0.17‰), and apply a source-melt fractionation of 0.05-0.08‰ (the largest isotopic fractionation predicted by our mantle melting models; Fig. 4). The results of our modelling indicate that the heaviest δ^{56}Fe value of a melt from a metasomatized peridotite is ~+0.22-0.25‰, approximately equivalent to the heaviest value measured in any of the GSC basalts. It is important to note, however, that this value is still too low to recreate the range of δ^{56}Fe compositions observed in the GSC basalts unless it is assumed that sample ST7-17D-1g (from 86.13°W) represents a pure (un-mixed) melt of the enriched mantle component alone (Fig. 6a). This is considered highly unlikely as this sample has a relatively low MgO concentration (6.83 wt%) and is therefore likely to have undergone significant homogenisation in sub-ridge magma storage regions (Shorttle et al., 2016). Therefore, melting of an isotopically heavy, metasomatized peridotite cannot recreate the δ^{56}Fe composition of the GSC basalts.

6.5 Lithological Heterogeneity

To investigate whether the Fe-isotope heterogeneity identified in the GSC basalts tracks lithological heterogeneity in the underlying mantle we use a simple 2-component mantle melting model (based on the Melt-PX model of Lambart et al., 2016) to simulate melting of a compositionally depleted peridotite and an enriched pyroxenite (Appendix A). The major-element composition of the pyroxenite component was set as the M5-40 composition from Lambart et al. (2013), a garnet websterite that lies close to the mean composition of the natural pyroxenite population (Appendix A). We model the trace-element composition of this component as a mixture between depleted

This manuscript has been accepted for publication in *Earth and Planetary Science Letters*. Please cite this article as: **Gleeson et al. (2020). Novel insights from Fe-isotopes into the lithological heterogeneity of Ocean Island Basalts and plume-influenced MORBS. *Earth and Planetary Science Letters*.** https://doi.org/10.1016/j.epsl.2020.116114

peridotitic mantle and recycled crustal components (see Appendix A for details). Other proposed compositions for mantle pyroxenites were tested and the results indicate that the δ^{56}Fe composition of the pyroxenite-derived melt that is estimated below represents a maximum value (i.e. by using other pyroxenitic compositions less heterogeneity in the Fe-isotope composition of the mantle source is required to explain our results; Fig S.4).

Our Melt-PX based mantle melting model was coupled to a MCMC algorithm (as described above) in order to estimate the proportion of pyroxenite-derived melt that contributes to each GSC basalt (Fig. 5). Our results allow us to estimate the δ^{56}Fe of the pure pyroxenite melt, which is required to explain the heterogeneity observed in the GSC basalts, when the concentration of Fe is: (i) equivalent in melts derived from the two components (δ^{56}Fe=+0.341±0.037‰); and (ii) ~1.5 times greater in melts derived from the pyroxenitic source component, which is reasonable given that melts of a pyroxenitic source often possess greater concentrations of FeO (Lambart et al., 2013) (δ^{56}Fe=+0.281±0.031‰; Fig. 6c). These estimates are remarkably similar to the heaviest δ^{56}Fe measured in any OIB globally (δ^{56}Fe=+0.31 - +0.34‰; Fig. 6c; Konter et al., 2016).

Our pyroxenite melting model also enables us to calculate the extent of Fe-isotope fractionation that is expected during melting of a peridotite-pyroxenite mantle (Fig. 5; Fig. 6). The δ^{56}Fe composition of the primary mantle melt formed at each pressure increment is calculated using theoretical and experimental constraints on Fe-O force constants in basaltic melt and mantle minerals (Dauphas et al., 2014; Sossi and O'Neill, 2017). As expected, the modelled δ^{56}Fe composition of melts from the pyroxenitic source are heavier than those from the peridotite source, especially if the resulting melts are assumed to be slightly more oxidised than those of a depleted peridotite (Fig. 4). Nevertheless, to generate the highest δ^{56}Fe compositions displayed by the GSC basalts we require the pyroxenitic source beneath the GSC to be isotopically-heavy (δ^{56}Fe=+0.18 - +0.20‰; Fig. 5; Fig. 6). This estimate is remarkably similar to the predicted composition of pyroxenitic material that forms due to

This manuscript has been accepted for publication in *Earth and Planetary Science Letters*. Please cite this article as: **Gleeson et al. (2020). Novel insights from Fe-isotopes into the lithological heterogeneity of Ocean Island Basalts and plume-influenced MORBS. *Earth and Planetary Science Letters*.** https://doi.org/10.1016/j.epsl.2020.116114

subduction and subsequent melting of isotopically heavy eclogite (Nebel et al., 2019), and is therefore considered as a reasonable estimate of the δ^{56}Fe composition of a mantle pyroxenite.

As a result, we suggest that the heterogeneity displayed by the GSC basalts is primarily driven by changes in the amount of pyroxenite-derived melt that is delivered to the sub-ridge magmatic sills/mush region. However, the presence of highly-enriched basalts, found only ~20km away from 'moderately' enriched basalts, in regions of the GSC where there is no increase in crustal thickness (e.g. TR164 26D-3g; Mittelstaedt et al., 2014) cannot be explained by an anomalously large flux of melts from a pyroxenitic source to that segment of the GSC. Since the models above simply evaluate the relative proportion of pyroxenite- and peridotite-derived melt that contributes to each sample, these highly-enriched basalts may instead represent the incomplete mixing of high-pressure pyroxenite-derived melts with those sourced from an isotopically-depleted peridotite at shallower levels (Gibson and Richards, 2018; Rudge et al., 2013). Our results have important implications for plume-ridge interaction globally as they show that short length-scale heterogeneities in the geochemical composition of plume-influenced basalts may result from incorporation of melts from a plume-derived pyroxenitic lithology.

7 IMPLICATIONS

7.1 LITHOLOGICAL HETEROGENEITY IN THE GALÁPAGOS MANTLE PLUME

Our new Fe-isotope data demonstrates that melts derived from a lithologically-distinct (i.e. pyroxenitic) component are present beneath the GSC. The relationship between lithological heterogeneity and heterogeneity in radiogenic isotope ratios in the Galapagos mantle plume is currently unclear (Vidito et al., 2013; Gleeson and Gibson, 2019). Here we attempt to constrain this uncertainty by establishing the radiogenic isotope composition of the enriched pyroxenitic plume component that is present beneath the GSC. We achieved this by iteratively adjusting the Sr, Nd and

This manuscript has been accepted for publication in *Earth and Planetary Science Letters*. Please cite this article as: **Gleeson et al. (2020). Novel insights from Fe-isotopes into the lithological heterogeneity of Ocean Island Basalts and plume-influenced MORBS. *Earth and Planetary Science Letters*.** https://doi.org/10.1016/j.epsl.2020.116114

Pb isotope composition of the enriched pyroxenitic plume component in our Melt-PX based mantle melting models until the observed trace-element and radiogenic isotope composition of the eastern GSC basalts are reproduced (Fig. 7; chemical variations are related to variations in the relative upwelling velocity of the mantle). In this analysis, we attempt to re-produce the composition of the eastern GSC basalts as their radiogenic isotopic compositions form from mixing of melts from only two-components, avoiding any complications caused by the presence of the WD plume component beneath the western GSC. Our results indicate that the measured Sr, Nd and Pb isotope ratios of the GSC basalts cannot be reproduced by melting of a mantle source with extremely-radiogenic Pb-isotope signatures (i.e. FLO; Fig. 7). Instead, our analysis suggests that this component has a moderately radiogenic Pb-isotope signature ($^{206}Pb/^{204}Pb$ ~19.17). We note that our proposed Pb isotopic composition for the enriched pyroxenite source is similar to that of mildly alkaline basalts from western Santiago (Gibson et al., 2012). These basalts also possess high FeO and low CaO whole-rock contents that are characteristic of experimental melts of silica-undersaturated pyroxenite lithologies (e.g. M5-40; Lambart et al., 2013; Fig. S.3) and may suggest that a lithologically distinct (and previously unidentified) central component exists in the Galápagos mantle plume (Fig. 1; Fig. 7). More work is required to confirm this hypothesis, but it is supported by the absence of evidence for lithological heterogeneity in each of the 4 previously identified mantle components in the Galápagos mantle plume (Gleeson and Gibson, 2019; Vidito et al., 2013).

7.2 GLOBAL IMPLICATIONS

The GSC basalts analysed in this study represent one of the first systematic studies of Fe-isotopes in a set of well-characterised oceanic basalts. Our new analyses reveal a large range in the $\delta^{56}Fe$ composition of the GSC basalts (+0.05 – +0.25‰), similar to a number of regions globally (e.g. Rochambeau Ridges in the Lau back-arc basin and Pitcairn; Fig. 8; Nebel et al., 2019, 2018). We have shown that this $\delta^{56}Fe$ heterogeneity is related to the lithological properties of the mantle source

This manuscript has been accepted for publication in *Earth and Planetary Science Letters*. Please cite this article as: **Gleeson et al. (2020). Novel insights from Fe-isotopes into the lithological heterogeneity of Ocean Island Basalts and plume-influenced MORBS. *Earth and Planetary Science Letters*.** https://doi.org/10.1016/j.epsl.2020.116114

beneath the GSC (Fig. 9), which has important implications for our understanding of published Fe-isotope datasets of oceanic basalts (Konter et al., 2016; Nebel et al., 2013; Teng et al., 2013). For example, our results indicate that the highest δ^{56}Fe values measured in basalts from Samoa may result from melting of a pyroxenitic component with little to no involvement of peridotite-derived melts (Konter et al., 2016). Interestingly, the heavy δ^{56}Fe component that has been identified in the Samoan (and Pitcairn) lavas have distinctly different Pb-isotope signatures than that identified in the GSC basalts, indicating that the high δ^{56}Fe signature in oceanic basalts is not related to the presence of a single mantle component (Konter et al., 2016; Nebel et al., 2019). In addition, the limited Fe-isotope data that exists for the Society Islands demonstrates that these basalts are notably heavier than most MORBs (Fig. 8; Weyer and Ionov, 2007). This may indicate the presence of a pyroxenitic component beneath these islands (as our models indicate that these moderately-heavy δ^{56}Fe compositions cannot be explained by lower melt extents or variations in fO_2), but more data is required to confirm this hypothesis. Similar observations can also be made for the Rochambeau Ridges in the Lau back-arc basin (Nebel et al., 2018).

Finally, a global compilation of MORB δ^{56}Fe compositions reveals a similar range to that observed in the GSC basalts (once the two most enriched samples are excluded; Nebel et al., 2013; Teng et al., 2013). The highest δ^{56}Fe values observed in MORBs (δ^{56}Fe ~ 0.17‰) are found in EMORBs from the FAMOUS segment of the Mid-Atlantic Ridge (between 35°50′ to 37°20′N; Nebel et al., 2013), which are influenced by the Azores mantle plume. We suggest that the range in δ^{56}Fe compositions displayed by global MORBs may represent varying contribution from enriched, pyroxenitic components. However, more data is required to understand how this might relate to melts sourced from nearby mantle plumes. We propose that analysis of plume-influenced MORBs may represent an effective way to constrain this relationship and identify the presence of pyroxenitic components in upwelling mantle plumes. Many plume-influenced ridges possess a number of very enriched basalts (as seen along the GSC) that represent an anomalously high contribution from melts of an

This manuscript has been accepted for publication in *Earth and Planetary Science Letters*. Please cite this article as: **Gleeson et al. (2020). Novel insights from Fe-isotopes into the lithological heterogeneity of Ocean Island Basalts and plume-influenced MORBS. *Earth and Planetary Science Letters*.** https://doi.org/10.1016/j.epsl.2020.116114

isotopically-enriched mantle source (Gibson and Richards, 2018). Therefore, Fe-isotope analysis of these basalts may provide a unique insight into the extent of lithological heterogeneity in the convecting mantle.

8 CONCLUSIONS

The range of δ^{56}Fe compositions measured in the basalts from the Galápagos Spreading Centre (+0.05 to +0.25‰) is remarkably similar to that observed elsewhere (e.g. Lau basin; Nebel et al., 2018). New considerations of Fe-isotope fractionation during mantle melting, alongside Monte Carlo simulations of adiabatic decompression melting beneath an oceanic spreading centre, are used to show that the large variation observed in the δ^{56}Fe composition of the GSC basalts cannot be related to melt fraction, the influence of isotopically-light garnet, or the fO_2 of a peridotitic source. However, we show that our new data is consistent with incorporation of melts from an isotopically-heavy pyroxenite source. In order to match the δ^{56}Fe composition of the GSC basalts our models indicate that this pyroxenitic component must have a source δ^{56}Fe composition of ~+0.18 - +0.20‰, remarkably similar to the δ^{56}Fe composition of secondary pyroxenites predicted by Nebel et al. (2019). Our results therefore indicate that the heterogeneity observed in the δ^{56}Fe composition of the GSC basalts relates to variations in the proportion of pyroxenite-derived melt.

Our results have several key implications for our understanding of lithological heterogeneity in the Galápagos mantle plume as well as beneath MORBs and OIBs globally. Firstly, our results highlight that Fe-isotopes may provide an effective tracer of lithological heterogeneity in the Earth's convecting mantle. Secondly, our new Fe-isotope data confirms that a pyroxenitic component exists in the Galápagos mantle, possibly as short length scale heterogeneities beneath the central Galápagos. Finally, comparison of our new δ^{56}Fe data, and our new models of Fe-isotope fractionation during mantle melting, to the limited published datasets that exists for OIBs (e.g. Society) and enriched

This manuscript has been accepted for publication in *Earth and Planetary Science Letters*. Please cite this article as: **Gleeson et al. (2020). Novel insights from Fe-isotopes into the lithological heterogeneity of Ocean Island Basalts and plume-influenced MORBS. *Earth and Planetary Science Letters*.** https://doi.org/10.1016/j.epsl.2020.116114

499 MORBs (e.g. FAMOUS on the Mid Atlantic Ridge) indicates that these basalts, with moderately-heavy

500 δ^{56}Fe compositions, contain a significant contribution from melts of a isotopically heavy pyroxenite.

501

502 ACKNOWLEDGEMENTS

503 This study was supported by a NERC (Natural Environmental Research Council) Research Training

504 Student Grant (NE/L002507/1) awarded to M.L.M.G as well as NERC grants RG57434 (S.A.G) and

505 NE/M00427/1 and NE/M010848/1 (H.M.W) and ERC Habitable Planet consolidator grant (306655;

506 H.M.W). We are grateful to Iris Buisman and Jason Day for their assistance with electron microprobe

507 and laser-ablation inductively-coupled mass spectrometry analysis, respectively. We also thank

508 Callum Reekie and Simon Matthews for their assistance with sample preparation for Fe-isotope

509 analysis, as well as Oli Nebel and an anonymous reviewer for their helpful and constructive

510 comments.

This manuscript has been accepted for publication in *Earth and Planetary Science Letters*. Please cite this article as: **Gleeson et al. (2020). Novel insights from Fe-isotopes into the lithological heterogeneity of Ocean Island Basalts and plume-influenced MORBS. *Earth and Planetary Science Letters*.** https://doi.org/10.1016/j.epsl.2020.116114

REFERENCES

Afonso, J.C., Fernàndez, M., Ranalli, G., Griffin, W.L., Connolly, J.A.D., 2008. Integrated geophysical-petrological modeling of the lithosphere and sublithospheric upper mantle: Methodology and applications. Geochem. Geophys. Geosystems 9, n/a-n/a. https://doi.org/10.1029/2007GC001834

Christie, D.M., Werner, R., Hauff, F., Hoernle, K., Hanan, B.B., 2005. Morphological and geochemical variations along the eastern Galápagos Spreading Center. Geochem. Geophys. Geosystems 6, n/a-n/a. https://doi.org/10.1029/2004GC000714

Cottrell, E., Kelley, K.A., 2011. The oxidation state of Fe in MORB glasses and the oxygen fugacity of the upper mantle. Earth Planet. Sci. Lett. 305, 270–282. https://doi.org/10.1016/j.epsl.2011.03.014

Craddock, P.R., Warren, J.M., Dauphas, N., 2013. Abyssal peridotites reveal the near-chondritic Fe isotopic composition of the Earth. Earth Planet. Sci. Lett. 365, 63–76. https://doi.org/10.1016/j.epsl.2013.01.011

Cushman, B., Sinton, J., Ito, G., Eaby Dixon, J., 2004. Glass compositions, plume-ridge interaction, and hydrous melting along the Galápagos Spreading Center, 90.5°W to 98°W. Geochem. Geophys. Geosystems 5. https://doi.org/10.1029/2004GC000709

Dauphas, N., Craddock, P.R., Asimow, P.D., Bennett, V.C., Nutman, A.P., Ohnenstetter, D., 2009. Iron isotopes may reveal the redox conditions of mantle melting from Archean to Present. Earth Planet. Sci. Lett. 288, 255–267. https://doi.org/10.1016/j.epsl.2009.09.029

Dauphas, N., Roskosz, M., Alp, E.E., Neuville, D.R., Hu, M.Y., Sio, C.K., Tissot, F.L.H., Zhao, J., Tissandier, L., Médard, E., Cordier, C., 2014. Magma redox and structural controls on iron isotope variations in Earth's mantle and crust. Earth Planet. Sci. Lett. 398, 127–140. https://doi.org/10.1016/j.epsl.2014.04.033

Davis, F.A., Humayun, M., Hirschmann, M.M., Cooper, R.S., 2013. Experimentally determined mineral/melt partitioning of first-row transition elements (FRTE) during partial melting of peridotite at 3GPa. Geochim. Cosmochim. Acta 104, 232–260. https://doi.org/10.1016/j.gca.2012.11.009

Detrick, R.S., Sinton, J.M., Ito, G., Canales, J.P., Behn, M., Blacic, T., Cushman, B., Dixon, J.E., Graham, D.W., Mahoney, J.J., 2002. Correlated geophysical, geochemical, and volcanological manifestations of plume-ridge interaction along the Galápagos Spreading Center. Geochem. Geophys. Geosystems 3, 1–14. https://doi.org/10.1029/2002GC000350

Gale, A., Langmuir, C.H., Dalton, C.A., 2014. The Global Systematics of Ocean Ridge Basalts and their Origin. J. Petrol. 55, 1051–1082. https://doi.org/10.1093/petrology/egu017

Gibson, S.A., Geist, D.G., Day, J.A., Dale, C.W., 2012. Short wavelength heterogeneity in the Galápagos plume: Evidence from compositionally diverse basalts on Isla Santiago. Geochem. Geophys. Geosystems 13. https://doi.org/10.1029/2012GC004244

Gibson, S.A., Geist, D.J., Richards, M.A., 2015. Mantle plume capture, anchoring, and outflow during Galápagos plume-ridge interaction: Mantle plume capture & outflow. Geochem. Geophys. Geosystems 16, 1634–1655. https://doi.org/10.1002/2015GC005723

Gibson, S.A., Richards, M.A., 2018. Delivery of deep-sourced, volatile-rich plume material to the global ridge system. Earth Planet. Sci. Lett. 499, 205–218. https://doi.org/10.1016/j.epsl.2018.07.028

Gleeson, M.L.M., Gibson, S.A., 2019. Crustal controls on apparent mantle pyroxenite signals in ocean-island basalts. Geology. https://doi.org/10.1130/G45759.1

Harpp, K.S., Geist, D.J., Koleszar, A.M., Christensen, B., Lyons, J., Sabga, M., Rollins, N., 2014. The Geology and Geochemistry of Isla Floreana, Galápagos: A Different Type of Late-Stage Ocean Island Volcanism, in: Harpp, K.S., Mittelstaedt, E., d'Ozouville, N., Graham, D.W. (Eds.),

This manuscript has been accepted for publication in *Earth and Planetary Science Letters*. Please cite this article as: **Gleeson et al. (2020). Novel insights from Fe-isotopes into the lithological heterogeneity of Ocean Island Basalts and plume-influenced MORBS. *Earth and Planetary Science Letters*.** https://doi.org/10.1016/j.epsl.2020.116114

559 Geophysical Monograph Series. John Wiley & Sons, Inc, Hoboken, New Jersey, pp. 71–117.
560 https://doi.org/10.1002/9781118852538.ch6
561 Harpp, K.S., White, W.M., 2001. Tracing a mantle plume: Isotopic and trace element variations of
562 Galápagos seamounts. Geochem. Geophys. Geosystems 2, n/a-n/a.
563 https://doi.org/10.1029/2000GC000137
564 Hart, S.R., Hauri, E.H., Oschmann, L.A., Whitehead, J.A., 1992. Mantle Plumes and Entrainment:
565 Isotopic Evidence. Science 256, 517–520. https://doi.org/10.1126/science.256.5056.517
566 Herzberg, C., 2011. Identification of Source Lithology in the Hawaiian and Canary Islands:
567 Implications for Origins. J. Petrol. 52, 113–146. https://doi.org/10.1093/petrology/egq075
568 Hoernle, K., Werner, R., Morgan, J.P., Garbe-Schönberg, D., Bryce, J., Mrazek, J., 2000. Existence of
569 complex spatial zonation in the Galápagos plume. Geology 28, 435.
570 https://doi.org/10.1130/0091-7613(2000)28<435:EOCSZI>2.0.CO;2
571 Hofmann, A.W., 1997. Mantle geochemistry: the message from oceanic volcanism. Nature 385, 219–
572 229. https://doi.org/10.1038/385219a0
573 Huang, F., Chakraborty, P., Lundstrom, C.C., Holmden, C., Glessner, J.J.G., Kieffer, S.W., Lesher, C.E.,
574 2010. Isotope fractionation in silicate melts by thermal diffusion. Nature 464, 396–400.
575 https://doi.org/10.1038/nature08840
576 Ingle, S., Ito, G., Mahoney, J.J., Chazey, W., Sinton, J., Rotella, M., Christie, D.M., 2010. Mechanisms
577 of geochemical and geophysical variations along the western Galápagos Spreading Center.
578 Geochem. Geophys. Geosystems 11, n/a-n/a. https://doi.org/10.1029/2009GC002694
579 Jackson, M.G., Hart, S.R., Saal, A.E., Shimizu, N., Kurz, M.D., Blusztajn, J.S., Skovgaard, A.C., 2008.
580 Globally elevated titanium, tantalum, and niobium (TITAN) in ocean island basalts with high ^{3}
581 He/ ^{4} He. Geochem. Geophys. Geosystems 9, n/a-n/a.
582 https://doi.org/10.1029/2007GC001876
583 Konter, J.G., Pietruszka, A.J., Hanan, B.B., Finlayson, V.A., Craddock, P.R., Jackson, M.G., Dauphas, N.,
584 2016. Unusual δ 56 Fe values in Samoan rejuvenated lavas generated in the mantle. Earth
585 Planet. Sci. Lett. 450, 221–232. https://doi.org/10.1016/j.epsl.2016.06.029
586 Kurz, M.D., Geist, D., 1999. Dynamics of the Galapagos hotspot from helium isotope geochemistry.
587 Geochim. Cosmochim. Acta 63, 4139–4156. https://doi.org/10.1016/S0016-7037(99)00314-
588 2
589 Lambart, S., Baker, M.B., Stolper, E.M., 2016. The role of pyroxenite in basalt genesis: Melt-PX, a
590 melting parameterization for mantle pyroxenites between 0.9 and 5 GPa: Melt-PX:
591 Pyroxenite Melting Model. J. Geophys. Res. Solid Earth 121, 5708–5735.
592 https://doi.org/10.1002/2015JB012762
593 Lambart, S., Koornneef, J.M., Millet, M.-A., Davies, G.R., Cook, M., Lissenberg, C.J., 2019. Highly
594 heterogeneous depleted mantle recorded in the lower oceanic crust. Nat. Geosci. 12, 482–
595 486. https://doi.org/10.1038/s41561-019-0368-9
596 Lambart, S., Laporte, D., Schiano, P., 2013. Markers of the pyroxenite contribution in the major-
597 element compositions of oceanic basalts: Review of the experimental constraints. Lithos
598 160–161, 14–36. https://doi.org/10.1016/j.lithos.2012.11.018
599 Lee, C.-T.A., Luffi, P., Plank, T., Dalton, H., Leeman, W.P., 2009. Constraints on the depths and
600 temperatures of basaltic magma generation on Earth and other terrestrial planets using new
601 thermobarometers for mafic magmas. Earth Planet. Sci. Lett. 279, 20–33.
602 https://doi.org/10.1016/j.epsl.2008.12.020
603 Matzen, A.K., Baker, M.B., Beckett, J.R., Wood, B.J., Stolper, E.M., 2017a. The effect of liquid
604 composition on the partitioning of Ni between olivine and silicate melt. Contrib. Mineral.
605 Petrol. 172. https://doi.org/10.1007/s00410-016-1319-8
606 Matzen, A.K., Wood, B.J., Baker, M.B., Stolper, E.M., 2017b. The roles of pyroxenite and peridotite in
607 the mantle sources of oceanic basalts. Nat. Geosci. 10, 530–535.
608 https://doi.org/10.1038/ngeo2968

This manuscript has been accepted for publication in *Earth and Planetary Science Letters*. Please cite this article as: **Gleeson et al. (2020). Novel insights from Fe-isotopes into the lithological heterogeneity of Ocean Island Basalts and plume-influenced MORBS. *Earth and Planetary Science Letters*.** https://doi.org/10.1016/j.epsl.2020.116114

McCoy-West, A.J., Fitton, J.G., Pons, M.-L., Inglis, E.C., Williams, H.M., 2018. The Fe and Zn isotope composition of deep mantle source regions: Insights from Baffin Island picrites. Geochim. Cosmochim. Acta 238, 542–562. https://doi.org/10.1016/j.gca.2018.07.021

Mittelstaedt, E., Soule, A.S., Harpp, K.S., Fornari, D., 2014. Variations in Crustal Thickness, Plate Rigidity, and Volcanic Processes Throughout the Northern Galápagos Volcanic Province, in: Harpp, K.S., Mittelstaedt, E., d'Ozouville, N., Graham, D.W. (Eds.), Geophysical Monograph Series. John Wiley & Sons, Inc, Hoboken, New Jersey, pp. 263–284. https://doi.org/10.1002/9781118852538.ch14

Nebel, O., Arculus, R.J., Sossi, P.A., Jenner, F.E., Whan, T.H.E., 2013. Iron isotopic evidence for convective resurfacing of recycled arc-front mantle beneath back-arc basins. Geophys. Res. Lett. 40, 5849–5853. https://doi.org/10.1002/2013GL057976

Nebel, O., Sossi, P.A., Bénard, A., Arculus, R.J., Yaxley, G.M., Woodhead, J.D., Rhodri Davies, D., Ruttor, S., 2019. Reconciling petrological and isotopic mixing mechanisms in the Pitcairn mantle plume using stable Fe isotopes. Earth Planet. Sci. Lett. 521, 60–67. https://doi.org/10.1016/j.epsl.2019.05.037

Nebel, O., Sossi, P.A., Foden, J., Bénard, A., Brandl, P.A., Stammeier, J.A., Lupton, J., Richter, M., Arculus, R.J., 2018. Iron isotope variability in ocean floor lavas and mantle sources in the Lau back-arc basin. Geochim. Cosmochim. Acta 241, 150–163. https://doi.org/10.1016/j.gca.2018.08.046

Prissel, K.B., Krawczynski, M.J., Nie, N.X., Dauphas, N., Couvy, H., Hu, M.Y., Alp, E.E., Roskosz, M., 2018. Experimentally determined effects of olivine crystallization and melt titanium content on iron isotopic fractionation in planetary basalts. Geochim. Cosmochim. Acta 238, 580–598. https://doi.org/10.1016/j.gca.2018.07.028

Putirka, K., Ryerson, F.J., Perfit, M., Ridley, W.I., 2011. Mineralogy and Composition of the Oceanic Mantle. J. Petrol. 52, 279–313. https://doi.org/10.1093/petrology/egq080

Rhodes, J.M., Huang, S., Frey, F.A., Pringle, M., Xu, G., 2012. Compositional diversity of Mauna Kea shield lavas recovered by the Hawaii Scientific Drilling Project: Inferences on source lithology, magma supply, and the role of multiple volcanoes. Geochem. Geophys. Geosystems 13, n/a-n/a. https://doi.org/10.1029/2011GC003812

Rudge, J.F., Maclennan, J., Stracke, A., 2013. The geochemical consequences of mixing melts from a heterogeneous mantle. Geochim. Cosmochim. Acta 114, 112–143. https://doi.org/10.1016/j.gca.2013.03.042

Schilling, J.-G., Fontignie, D., Blichert-Toft, J., Kingsley, R., Tomza, U., 2003. Pb-Hf-Nd-Sr isotope variations along the Galápagos Spreading Center (101°-83°W): Constraints on the dispersal of the Galápagos mantle plume. Geochem. Geophys. Geosystems 4. https://doi.org/10.1029/2002GC000495

Schuessler, J.A., Schoenberg, R., Sigmarsson, O., 2009. Iron and lithium isotope systematics of the Hekla volcano, Iceland — Evidence for Fe isotope fractionation during magma differentiation. Chem. Geol. 258, 78–91. https://doi.org/10.1016/j.chemgeo.2008.06.021

Shorttle, O., Maclennan, J., Lambart, S., 2014. Quantifying lithological variability in the mantle. Earth Planet. Sci. Lett. 395, 24–40. https://doi.org/10.1016/j.epsl.2014.03.040

Shorttle, O., Rudge, J.F., Maclennan, J., Rubin, K.H., 2016. A Statistical Description of Concurrent Mixing and Crystallization during MORB Differentiation: Implications for Trace Element Enrichment. J. Petrol. 57, 2127–2162. https://doi.org/10.1093/petrology/egw056

Sobolev, A.V., Hofmann, A.W., Kuzmin, D.V., Yaxley, G.M., Arndt, N.T., Chung, S.-L., Danyushevsky, L.V., Elliott, T., Frey, F.A., Garcia, M.O., Gurenko, A.A., Kamenetsky, V.S., Kerr, A.C., Krivolutskaya, N.A., Matvienkov, V.V., Nikogosian, I.K., Rocholl, A., Sigurdsson, I.A., Sushchevskaya, N.M., Teklay, M., 2007. The Amount of Recycled Crust in Sources of Mantle-Derived Melts 316, 7.

This manuscript has been accepted for publication in *Earth and Planetary Science Letters*. Please cite this article as: **Gleeson et al. (2020). Novel insights from Fe-isotopes into the lithological heterogeneity of Ocean Island Basalts and plume-influenced MORBS. *Earth and Planetary Science Letters*.** https://doi.org/10.1016/j.epsl.2020.116114

Sorbadere, F., Laurenz, V., Frost, D.J., Wenz, M., Rosenthal, A., McCammon, C., Rivard, C., 2018. The behaviour of ferric iron during partial melting of peridotite. Geochim. Cosmochim. Acta 239, 235–254. https://doi.org/10.1016/j.gca.2018.07.019

Sossi, P.A., Foden, J.D., Halverson, G.P., 2012. Redox-controlled iron isotope fractionation during magmatic differentiation: an example from the Red Hill intrusion, S. Tasmania. Contrib. Mineral. Petrol. 164, 757–772. https://doi.org/10.1007/s00410-012-0769-x

Sossi, P.A., Nebel, O., Foden, J., 2016. Iron isotope systematics in planetary reservoirs. Earth Planet. Sci. Lett. 452, 295–308. https://doi.org/10.1016/j.epsl.2016.07.032

Sossi, P.A., O'Neill, H.St.C., 2017. The effect of bonding environment on iron isotope fractionation between minerals at high temperature. Geochim. Cosmochim. Acta 196, 121–143. https://doi.org/10.1016/j.gca.2016.09.017

Sun, S. -s., McDonough, W.F., 1989. Chemical and isotopic systematics of oceanic basalts: implications for mantle composition and processes. Geol. Soc. Lond. Spec. Publ. 42, 313–345. https://doi.org/10.1144/GSL.SP.1989.042.01.19

Teng, F.-Z., Dauphas, N., Helz, R.T., 2008. Iron Isotope Fractionation During Magmatic Differentiation in Kilauea Iki Lava Lake. Science 320, 1620–1622. https://doi.org/10.1126/science.1157166

Teng, F.-Z., Dauphas, N., Helz, R.T., Gao, S., Huang, S., 2011. Diffusion-driven magnesium and iron isotope fractionation in Hawaiian olivine. Earth Planet. Sci. Lett. 308, 317–324. https://doi.org/10.1016/j.epsl.2011.06.003

Teng, F.-Z., Dauphas, N., Huang, S., Marty, B., 2013. Iron isotopic systematics of oceanic basalts. Geochim. Cosmochim. Acta 107, 12–26. https://doi.org/10.1016/j.gca.2012.12.027

van der Hilst, R.D., Widiyantoro, S., Engdahl, E.R., 1997. Evidence for deep mantle circulation from global tomography. Nature 386, 578–584. https://doi.org/10.1038/386578a0

Vidito, C., Herzberg, C., Gazel, E., Geist, D., Harpp, K., 2013. Lithological structure of the Galápagos Plume: Lithological Structure Galpagos Plume. Geochem. Geophys. Geosystems 14, 4214–4240. https://doi.org/10.1002/ggge.20270

Villagómez, D.R., Toomey, D.R., Geist, D.J., Hooft, E.E.E., Solomon, S.C., 2014. Mantle flow and multistage melting beneath the Galápagos hotspot revealed by seismic imaging. Nat. Geosci. 7, 151–156. https://doi.org/10.1038/ngeo2062

Weyer, S., Ionov, D.A., 2007. Partial melting and melt percolation in the mantle: The message from Fe isotopes. Earth Planet. Sci. Lett. 259, 119–133. https://doi.org/10.1016/j.epsl.2007.04.033

White, W.M., McBirney, A.R., Duncan, R.A., 1993. Petrology and geochemistry of the Galápagos Islands: Portrait of a pathological mantle plume. J. Geophys. Res. Solid Earth 98, 19533–19563. https://doi.org/10.1029/93JB02018

Williams, H.M., Bizimis, M., 2014. Iron isotope tracing of mantle heterogeneity within the source regions of oceanic basalts. Earth Planet. Sci. Lett. 404, 396–407. https://doi.org/10.1016/j.epsl.2014.07.033

Williams, H.M., Nielsen, S.G., Renac, C., Griffin, W.L., O'Reilly, S.Y., McCammon, C.A., Pearson, N., Viljoen, F., Alt, J.C., Halliday, A.N., 2009. Fractionation of oxygen and iron isotopes by partial melting processes: Implications for the interpretation of stable isotope signatures in mafic rocks. Earth Planet. Sci. Lett. 283, 156–166. https://doi.org/10.1016/j.epsl.2009.04.011

Yaxley, G.M., Green, D.H., 1998. Reactions between eclogite and peridotite: mantle refertilisation by subduction of oceanic crust. Schweiz Miner. Petrogr Mitt 78, 243–255.

Zhao, X., Zhang, Z., Huang, S., Liu, Y., Li, X., Zhang, H., 2017. Coupled extremely light Ca and Fe isotopes in peridotites. Geochim. Cosmochim. Acta 208, 368–380. https://doi.org/10.1016/j.gca.2017.03.024

This manuscript has been accepted for publication in *Earth and Planetary Science Letters*. Please cite this article as: **Gleeson et al. (2020). Novel insights from Fe-isotopes into the lithological heterogeneity of Ocean Island Basalts and plume-influenced MORBS. *Earth and Planetary Science Letters*.** https://doi.org/10.1016/j.epsl.2020.116114

FIGURES

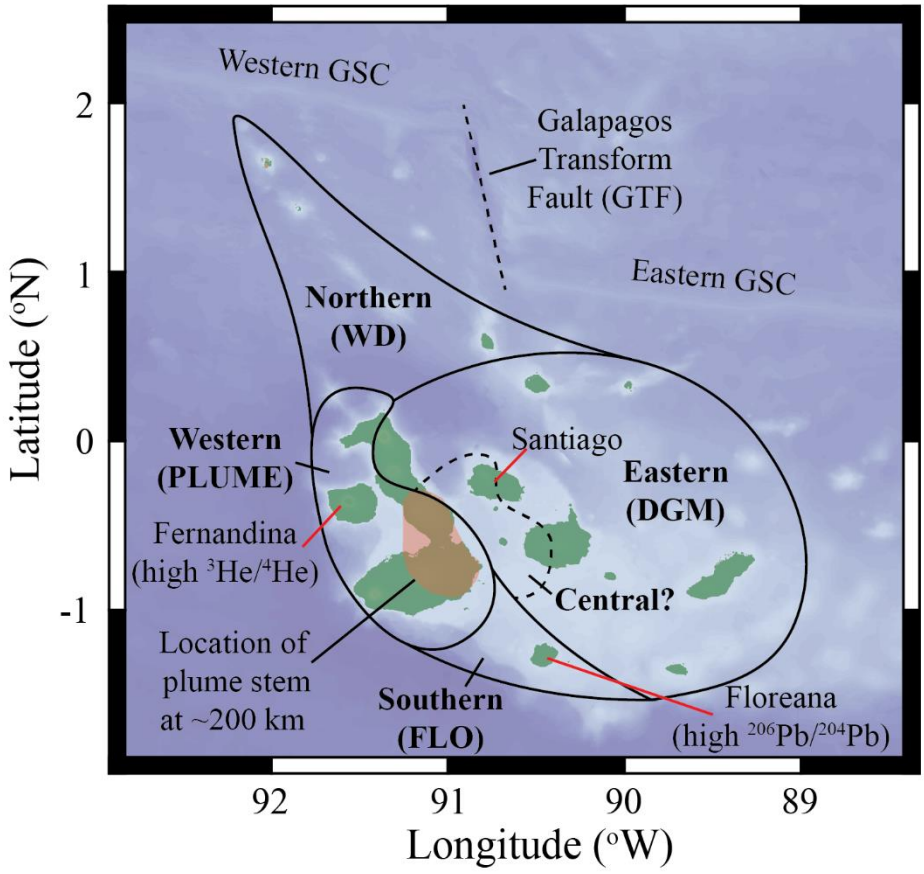

Figure 1 – Map of the Galápagos Archipelago highlighting the geographic distribution of the 4 isotopic components that have been previously identified on the basis of Sr, Nd, Pb and He isotopes (adapted from Hoernle et al., 2000). These components approximate correspond to the FLO, DGM, WD, and PLUME components identified by Harpp and White (2001). We have also included a region which we term the central isotopic component. This represents the region of the Galápagos archipelago where a pyroxenitic signature is apparent in the major-element chemistry of mildly-alkaline basalts that are isotopically similar to the enriched mantle component identified beneath the Galápagos Spreading Centre (Appendix A; see Section 7). The location of the mantle plume at 200km depth is from the seismic tomography study of Villagómez et al. (2014).

This manuscript has been accepted for publication in *Earth and Planetary Science Letters*. Please cite this article as: **Gleeson et al. (2020). Novel insights from Fe-isotopes into the lithological heterogeneity of Ocean Island Basalts and plume-influenced MORBS. *Earth and Planetary Science Letters*.** https://doi.org/10.1016/j.epsl.2020.116114

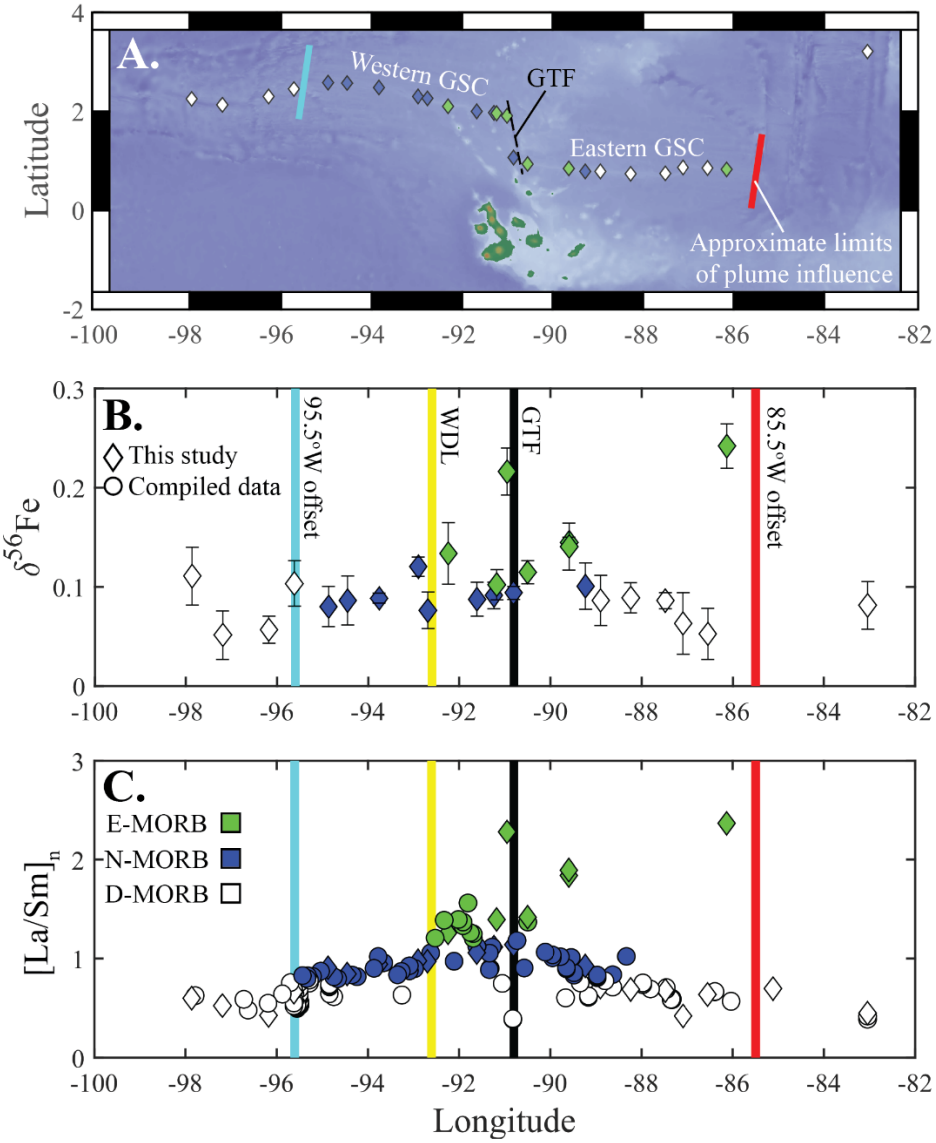

Figure 2 – Longitudinal variation in key geochemical parameters on the GSC. Panel **A.** shows the location of the samples analysed in this study and the region of the Galápagos spreading centre that is believed to be influenced by the Galápagos mantle plume (Gibson and Richards, 2018). Panel **B.** shows the range of δ^{56}Fe compositions measured in the GSC basalts. Panel **C.** shows the variation in $[La/Sm]_n$; the samples shown are colour coded according to their composition. In this study E-MORBs are defined as any basalt with a $[La/Sm]_n$ ratio greater than 1.2, D-MORBs are defined as any basalt where the $[La/Sm]_n$ ratio is less than 0.8 (where the n represents normalisation to the primitive mantle value of Sun and McDonough, (1989)).

This manuscript has been accepted for publication in *Earth and Planetary Science Letters*. Please cite this article as: **Gleeson et al. (2020). Novel insights from Fe-isotopes into the lithological heterogeneity of Ocean Island Basalts and plume-influenced MORBS. *Earth and Planetary Science Letters*.** https://doi.org/10.1016/j.epsl.2020.116114

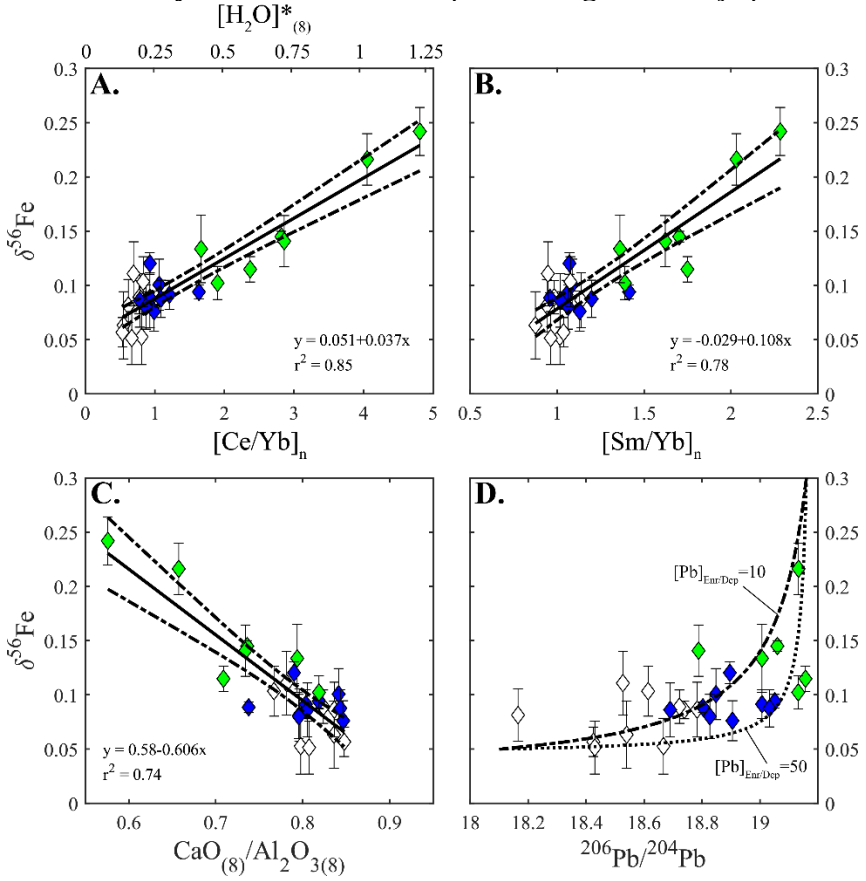

Figure 3 – Key correlations are observed between major- and trace-element parameters and the $\delta^{56}Fe$ composition of the GSC basalts. The strongest correlations are seen between $\delta^{56}Fe$ and REE ratios (**A.** and **B.**). We have used the $[Ce/Yb]_n$ composition of the GSC basalts to estimate their H_2O content at 8 wt% MgO (termed $[H_2O]^*_{(8)}$) following the method outlined in Gibson and Richards (2018). Panel **C.** shows the correlation between $\delta^{56}Fe$ and the fractionation corrected CaO/Al_2O_3 composition of the GSC basalts. This relationship may be indicative of a link between $\delta^{56}Fe$ and lithological heterogeneity in the sub-ridge mantle. Panel **D.** shows the relationship between $\delta^{56}Fe$ and $^{206}Pb/^{204}Pb$. Mixing curves between an enriched and depleted melt indicate that the lack of any significant correlation is expected in this case. All plots shown display the measured $\delta^{56}Fe$ data (i.e. uncorrected for fractional crystallisation). It is, however, important to note that these correlations are unchanged by the fractional crystallisation correction applied in this study. In other words, these correlations do not represent artefacts of fractional crystallisation.

This manuscript has been accepted for publication in *Earth and Planetary Science Letters*. Please cite this article as: **Gleeson et al. (2020). Novel insights from Fe-isotopes into the lithological heterogeneity of Ocean Island Basalts and plume-influenced MORBS. *Earth and Planetary Science Letters*.** https://doi.org/10.1016/j.epsl.2020.116114

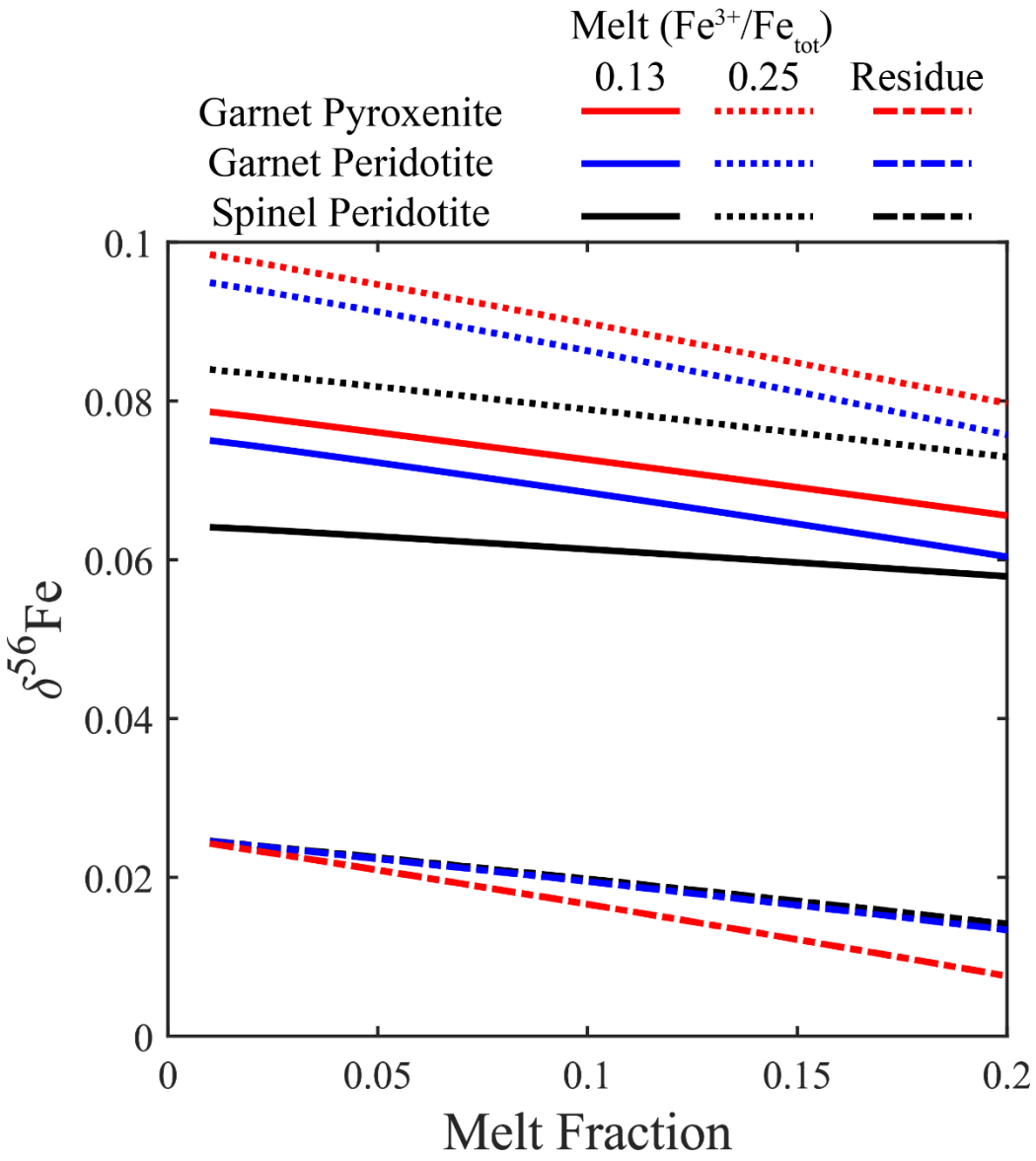

740

741 **Figure 4 -** Fe-isotope composition predicted during fractional melting of (i) Garnet peridotite; (ii)
742 spinel peridotite; and (iii) garnet pyroxenite. Melts of a garnet pyroxenite are predicted to be
743 marginally heavier than those of a spinel peridotite, but this variation is not large enough to explain
744 the heterogeneity in the composition of the GSC basalts. A larger difference is seen due to variations
745 in the Fe^{3+}/Fe_{tot} ratio of the resulting melt, but this is still not large enough to explain the
746 heterogeneity observed in the GSC basalts. For these calculations we take melting equations and
747 FeO contents from Williams and Bizimis (2014) for spinel peridotites and garnet pyroxenites and
748 from Afonso et al. (2008) for garnet peridotites.

This manuscript has been accepted for publication in *Earth and Planetary Science Letters*. Please cite this article as: **Gleeson et al. (2020). Novel insights from Fe-isotopes into the lithological heterogeneity of Ocean Island Basalts and plume-influenced MORBS. *Earth and Planetary Science Letters*.** https://doi.org/10.1016/j.epsl.2020.116114

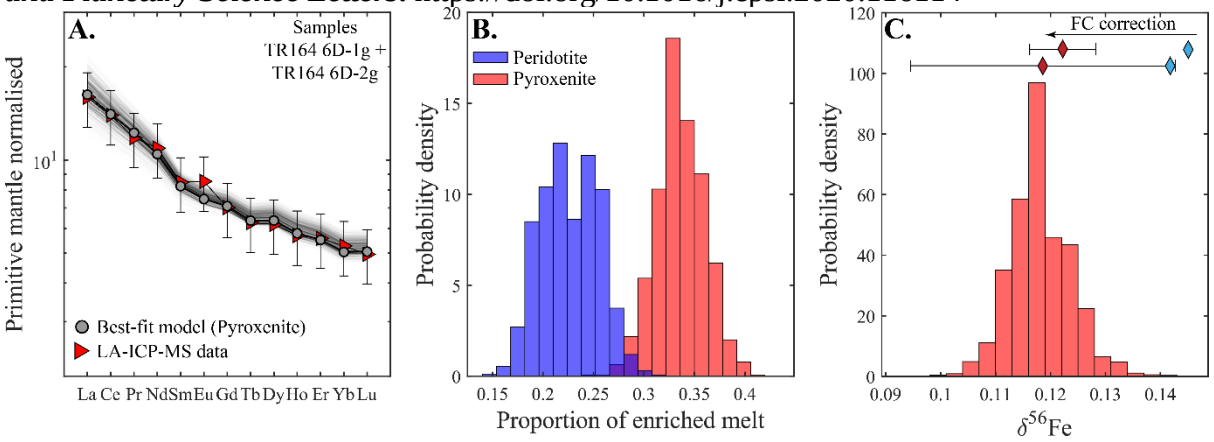

Figure 5 – Results of our mantle melting models. Panel **A.** shows the average trace-element composition of samples TR164 6D-1g and TR164 6D-2g (chosen as these represent E-MORBs with moderately elevated δ^{56}Fe signatures) and the trace-element composition of mantle melts predicted by our mantle melting models (grey lines). In this case all model compositions that are shown represent the compositions predicted by melting of a mantle that contains a pyroxenitic component and the grey circles represent the model that shows the closest match to the trace-element data of these two samples. Panel **B.** shows probability distributions for the proportion of enriched melt that is required to explain the composition of these samples when: (i) a 2-peridotite mantle is used (blue); and (ii) a peridotite-pyroxenite mantle is used (red). Panel **C.** shows the Fe-isotope composition predicted by melting a peridotite-pyroxenite mantle (see Methods for details of calculations). In this case the peridotite is assigned a δ^{56}Fe value of +0.01‰ (consistent with the highly depleted trace-element composition predicted for this component), and the pyroxenitic component is given a δ^{56}Fe composition of +0.20‰. The δ^{56}Fe composition predicted by our models provides an accurate match to the δ^{56}Fe composition measured in these two samples (red = fractionation corrected data; blue = raw data).

This manuscript has been accepted for publication in *Earth and Planetary Science Letters*. Please cite this article as: **Gleeson et al. (2020). Novel insights from Fe-isotopes into the lithological heterogeneity of Ocean Island Basalts and plume-influenced MORBS. *Earth and Planetary Science Letters*.** https://doi.org/10.1016/j.epsl.2020.116114

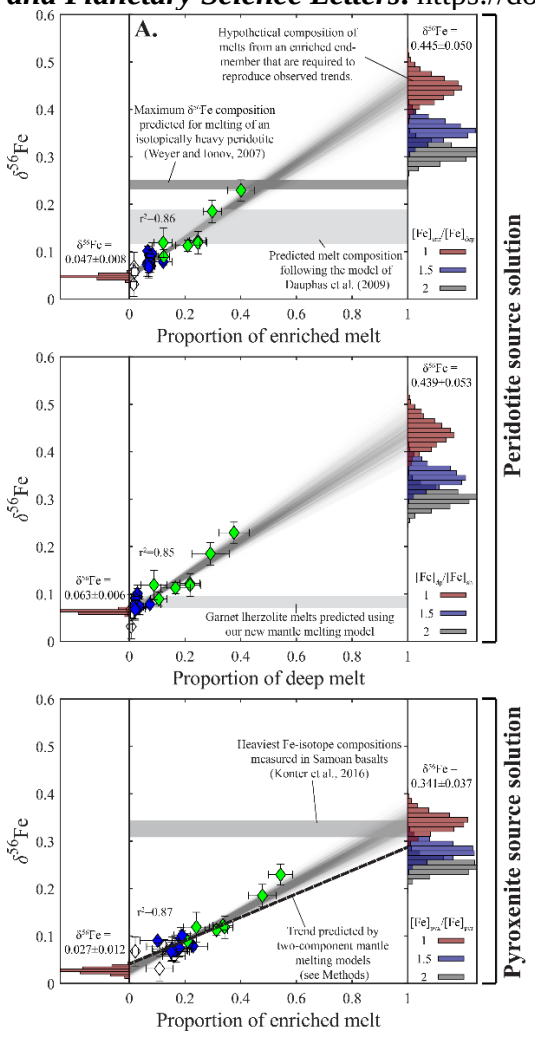

Figure 6 – The results of our Monte Carlo mantle melting models for a peridotite source (**A.** and **B.**) and pyroxenite source solution (**C.**) are shown. The composition of the end-member melts (shown by the histograms on each graph) were calculated by generating 1000 regression lines through the data where on every iteration each sample was positioned randomly according to their uncertainties. These results indicate that the δ^{56}Fe composition of enriched and/or deep melts that are required to explain the δ^{56}Fe heterogeneity in the GSC basalts (assuming a peridotitic source) are far heavier than predicted by any reasonable model of mantle melting. This analysis was carried out for scenarios where the concentration of Fe in the enriched (or deep) melt is assumed to be: (i) equivalent to (red); (ii) 1.5 times greater than (blue); or (iii) 2 times greater than (grey) that in the depleted (or shallow) melt.

This manuscript has been accepted for publication in *Earth and Planetary Science Letters*. Please cite this article as: **Gleeson et al. (2020). Novel insights from Fe-isotopes into the lithological heterogeneity of Ocean Island Basalts and plume-influenced MORBS. *Earth and Planetary Science Letters*.** https://doi.org/10.1016/j.epsl.2020.116114

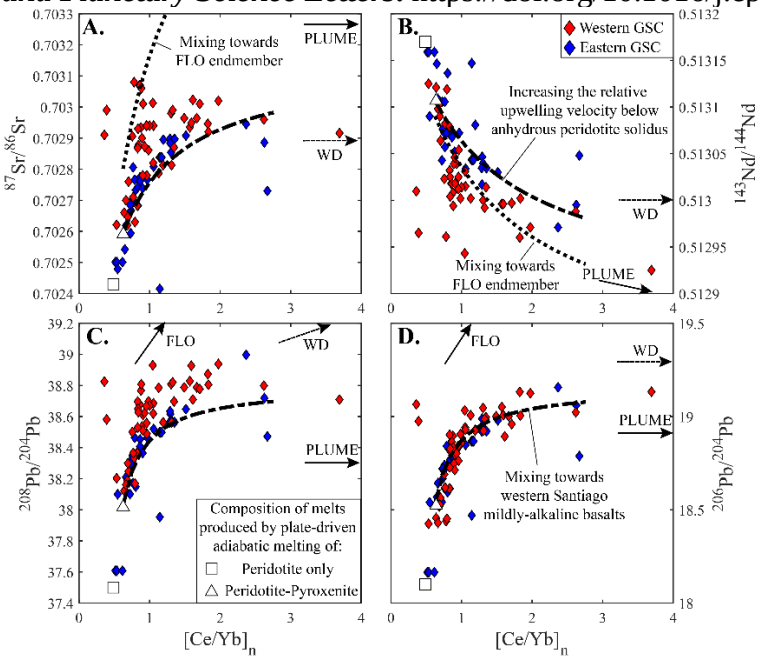

778

779 **Figure 7 –** Radiogenic isotope compositions of the GSC basalts plotted against trace-element
780 enrichment $[Ce/Yb]_n$. The western GSC basalts are shown by red symbols and the eastern GSC
781 symbols are shown by the blue symbols. The offset of the western and eastern GSC samples in Sr, Nd
782 and Pb isotope space is due to the incorporation of a LREE-enriched component in the shallow
783 mantle beneath the western GSC (WD component). Black lines show the radiogenic-isotope
784 composition predicted by our mantle melting models as the rate of mantle upwelling below the
785 anhydrous peridotite solidus is progressively increased. The dashed line represents a scenario where
786 the enriched end-member has an moderately radiogenic Pb and Sr isotopic composition. In this
787 scenario, and a very good match between the GSC data and the model predictions is observed
788 ($^{206}Pb/^{204}Pb$ = 19.17 and $^{208}Pb/^{204}Pb$ = 38.81, equivalent to the most radiogenic Pb-isotope
789 composition measured in any of the mildly alkaline basalts from Isla Santiago; Gibson et al., 2012).
790 Our analysis also demonstrates that the FLO mantle component from Harpp and White (2001) does
791 not contribute to the composition of the GSC basalts (dotted lines in panels **A.** and **B.**). Vectors
792 displayed in all panels are directed towards where the radiogenic isotope composition of the
793 Galápagos plume components intersect the right-hand y-axis ($[Ce/Yb]_n$).

This manuscript has been accepted for publication in *Earth and Planetary Science Letters*. Please cite this article as: **Gleeson et al. (2020). Novel insights from Fe-isotopes into the lithological heterogeneity of Ocean Island Basalts and plume-influenced MORBS. *Earth and Planetary Science Letters*.** https://doi.org/10.1016/j.epsl.2020.116114

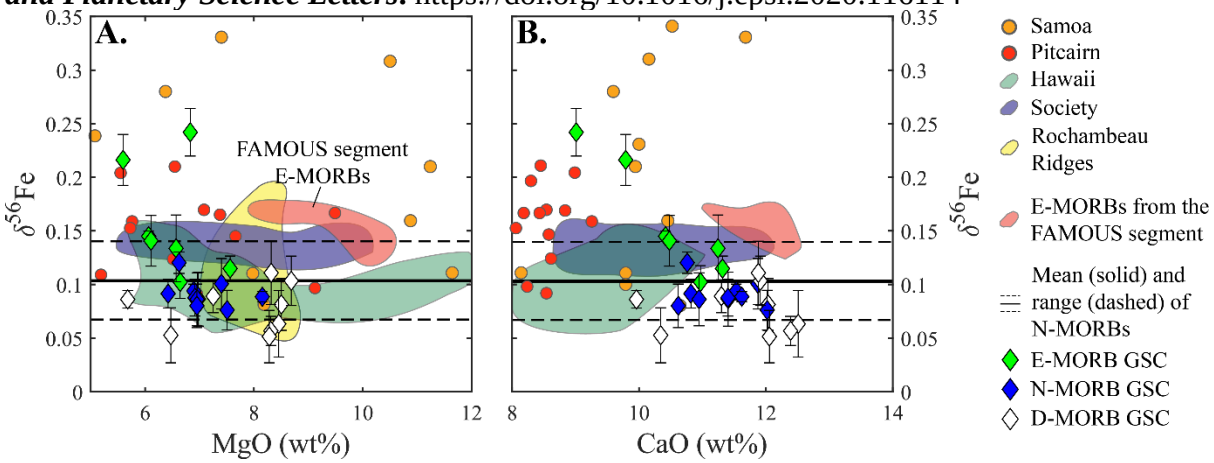

Figure 8 – Stable Fe-isotope variations in global oceanic basalts plotted against major-element parameters. It can be seen that the enriched MORBs from the FAMOUS segment plot at the upper end of the MORB field (Nebel et al., 2013; Teng et al., 2013), potentially indicating that these enriched samples may contain a significant contribution from a pyroxenitic source component. In addition, Fe-isotope compositions measured in basalts from various OIBs have significantly elevated values that may indicate the presence of a pyroxenite component in the mantle source. Data from (Konter et al., 2016; Nebel et al., 2019, 2018; Teng et al., 2013, 2008; Weyer and Ionov, 2007).

This manuscript has been accepted for publication in *Earth and Planetary Science Letters*. Please cite this article as: **Gleeson et al. (2020). Novel insights from Fe-isotopes into the lithological heterogeneity of Ocean Island Basalts and plume-influenced MORBS. *Earth and Planetary Science Letters*.** https://doi.org/10.1016/j.epsl.2020.116114

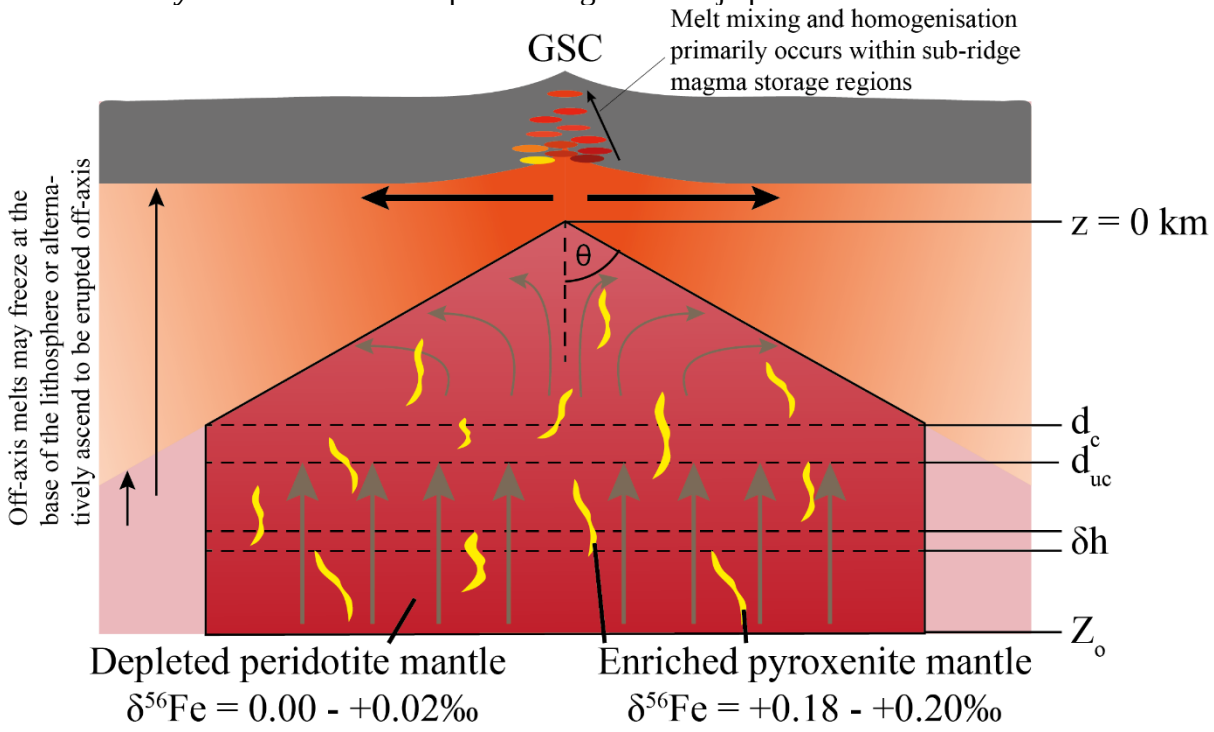

Figure 9 – Schematic illustration displaying the conceptual model by which the composition of melts from a 2-component mantle were calculated (see Appendix A for details). This shows a depth (d_c) below which the melting region (from which melts are extracted to be pooled at the ridge axis) is rectangular, a depth (d_{uc}) below which the relative upwelling velocity of the mantle is >1, and an incremental depth (δh) that represents the depth interval at which melt compositions were calculated in our model. This diagram also shows a key feature of our model, in that the sub-ridge mantle contains streaks and/or blebs of pyroxenitic material set in a peridotite matrix. Melt mixing and homogenisation is believed to occur in sub-ridge magma storage regions as recent studies have shown that the isotopic heterogeneity of melt entering the crust beneath oceanic spreading centres is very large (Lambart et al., 2019).

Appendix: Novel insights from Fe-isotopes into the lithological heterogeneity of Ocean Island Basalts and plume-influenced MORBs

Matthew L. M. Gleeson[1], **Sally A. Gibson**[1], **and Helen M. Williams**[1]

[1]Department of Earth Sciences, University of Cambridge,
Downing Street, Cambridge, UK, CB2 3EQ

mlmg3@cam.ac.uk

1. Modelling mantle melting

1.1. Simulating a 2-component mantle

We simulate melting of a two-component mantle (enriched 'blebs' suspended in a matrix of depleted and relatively refractory mantle peridotite) where the enriched component may be represented by either a relatively hydrous peridotite ($\sim$280-300 ppm H_2O) or a fusible pyroxene-rich lithology. In our models the composition of the depleted mantle component beneath the eastern GSC was set as the depleted DMM estimate from Workman and Hart (Workman and Hart, 2005), as their estimate for the trace-element composition of the average DMM was not able to reproduce the highly depleted nature of D-MORBs from the GSC.

Several lines of evidence indicate that the melt-source region beneath the western GSC is influenced by the presence of a LREE enriched source (i.e. D-MORBs are not observed along the western GSC), and Sr, Nd and Pb radiogenic isotope ratios reveal a significant contribution from the Wolf-Darwin (Northern) component along this ridge segment. As a result, the depleted/refractory mantle component beneath the western GSC cannot be assigned the same composition as that beneath the eastern GSC (Ingle et al., 2010). The trace-element composition of the depleted/refractory mantle component beneath the western GSC was therefore calculated as a mixture between the eastern GSC depleted mantle composition and the enriched mantle estimate of Donnelly et al. (2004) in a 0.9:0.1 ratio. This represents a non-unique solution to the composition of the depleted mantle component beneath the western GSC but is chosen here to represent incorporation of the Wolf-Darwin mantle component in the western GSC mantle as it reproduces the LREE enriched signature and high Ba/Nb ratio of these basalts.

For models where the enriched mantle component is represented by a relatively hydrous peridotite (280-300 ppm H_2O), the trace-element composition of this component was set as the Sun and McDonough (1989) estimate for the primitive mantle. In these (2-peridotite) models we initially simulated melting of the anhydrous mantle component during adiabatic ascent and then modelled the melting of the enriched mantle component along the P-T path defined by melting during adiabatic ascent of the anhydrous components (following the method of Rudge et al., 2013). As the anhydrous component accounts for 90% of the sub-ridge mantle (by mass) in most models it is reasonable to assume that the mantle P-T path is unlikely to be significantly influenced by cooling generated by the latent heat of melting of the hydrous mantle component. For these models of a 2-component peridotite, all calculations (including calculations of the trace-element

composition produced by near fractional melting at each pressure interval) were carried out using the pHMELTS algorithm (Asimow et al., 2004).

To simulate melting of a 2-component mantle that includes a pyroxenitic component we use the Melt-PX program of Lambart et al. (2016) to estimate the melt fraction vs depth curves for the peridotite and pyroxenite components we then calculate the trace-element composition of the melts formed at each depth using non-modal batch melting equations from Williams and Bizimis (2014). The major-element composition of the pyroxenite component was set as the M5-40 composition from Lambart et al. (2013), a garnet websterite that lies close to the mean composition of the natural pyroxenite population (experimental melts of this lithology possess major-element compositions that are very similar to those observed in the mildly alkaline basalts from western Santiago - see below). The trace-element composition is generally treated as a 50:50 mixture of the depleted mantle (Workman and Hart, 2005) and recycled oceanic crust (Porter and White, 2009), although other estimates may be relevant and were tested without any change in the results of this study (e.g. Lambart, 2017). For all models partition coefficients were taken from the lattice strain model of Gibson and Geist (2010).

Our model is designed so that changes in the chemistry of the erupted basalts are primarily controlled by variations in the relative mantle upwelling velocity (Ur) beneath the ridge (Cushman et al., 2004; Ingle et al., 2010). Large changes in the rate of mantle upwelling are predicted to occur at depths near the anhydrous peridotite solidus, as dehydration of olivine is believed to result in a significant increase in mantle viscosity (Hirth and Kohlstedt, 2003). Velocity profiles are modelled following the method of Ingle et al. (2010). Other factors that may influence the trace-element composition of the resulting melts (e.g. proportion of enriched material in the source, depth to the top of the melt column) were also considered.

The influence that these factors have on melt chemistry was investigated using a Markov Chain Monte Carlo algorithm (with 5000 iterations). In each model the maximum upwelling velocity, proportion of enriched material in the mantle source, width from which melts are pooled, and depth to the top of the melt column were randomly sampled within pre-set bounds. For each model the differences between the REE concentrations predicted by the mantle melting model (see below) and the observed REE concentrations in the GSC basalts were calculated. These differences were used to calculate an 'Acceptance Ratio' where 1 represents a perfect match between the model and data and 0 indicates no match between the model and data. The acceptance ratio is calculated using the following method:

$$AR = exp(-\sum_{i=1}^{n} \frac{|[C]_i - [\bar{C}]_i}{2[\hat{C}]_i})$$

Where $[C]_i$ is the concentration of trace-element i in the model; $[\bar{C}]_i$ is the concentration of the same trace-element in the sample under consideration; $[\hat{C}]_i$ is the analytical uncertainty for that trace-element; and n is the number of trace-elements under consideration. The results of the 5000 model iterations are then used to construct density distributions for the different parameters (i.e. determine which combination of parameters gives the best match to the trace-element composition of that sample). This method also allows us to construct an estimate (including uncertainties) for parameters such as the proportion

of enriched melt that is required to explain the trace-element signature of each sample.

1.2. Constraining melt compositions (calculating aggregated melts)

In this section we describe the method by which aggregate melt compositions are calculated following near-fractional melting of a two-component mantle (we assume that the instantaneous composition of the melts formed at each depth are known and/or previously calculated).

In our model we simulate melting of a two-component mantle in a triangular melting region beneath a mid-ocean ridge. As recent studies have shown that melts produced at large horizontal distance from the ridge axis may not be transported to the axial magma chamber and effectively pooled (Behn and Grove, 2015) we split our melting region into an upper triangular region and a lower rectangular region, with the transition at depth d_c. This effectively simulates a scenario where melts produced at horizontal distances greater than $d_c * tan(\theta)$ from the ridge axis are not pooled, and therefore do not contribute to the composition of the erupted melts. θ represents the angle between the mid-plane of the melting region and the base of the lithosphere. This scenario is shown schematically in Fig 8.

The aggregated melt compositions are then calculated using the following method:

Firstly, we define a height δh, which represents the pressure interval at which the melt-fraction is calculated in pHMELTS and Melt-PX ($10MPa$). This equates to approximately $309m$ if a density of $3300kg/m^3$ is used for the mantle. We then denote the volume of mantle between height h and $h + \delta h$ as v_i. We define v_i in two ways. For depths greater than d_c:

$$v_i = 2 * \delta h * d_c * tan(\theta)$$

and for depths shallower than d_c:

$$v_i = 2 * \delta h * (d_c - (n + 0.5) * \delta h) * tan(\theta)$$

where $n = 0$ at $z = d_c$, and represents the number of height increments (δh) above the transition from a triangular to a rectangular melting regime.

Additionally, we also define the voume of the triangular melting region (V_{top}) and rectangular melting region (V_{bottom}) as:

$$V_{top} - d_c^2 * tan(\theta)$$

and

$$V_{bottom} = 2 * d_c * tan(\theta) * (Z_o - d_c)$$

where Z_o is the maximum depth at which melting of either mantle component occurs.

We then ratio the volume at each incremental height to the volume of the triangular melting regime.

For depths shallower than d_c:

$$\frac{v_i}{V_{top}} = \frac{2 * \delta h * (d_c - (n + 0.5) * \delta h)}{d_c^2}$$

For depths greater than d_c:

$$\frac{v_i}{V_{top}} = \frac{2 * \delta h}{d_c}$$

By calculating the ratio between the volume of the triangular melting regime and the volume of the entire melting region, we are then able to raito the volume at each height increment to the total volume of the melting region:

$$V_{total} = d_c * tan(\theta) * (d_c + 2 * (Z_o - d_c))$$

$$\frac{V_{top}}{V_{total}} = \frac{d_c}{d_c + 2 * (Z_o - d_c)}$$

Therefore, for depths shallower than d_c:

$$\frac{v_i}{V_{total}} = \frac{V_{top}}{V_{total}} * \frac{v_i}{V_{top}} = \frac{2 * \delta h * (d_c - (n + 0.5) * \delta h)}{d_c * (d_c + 2 * (Z_o - d)c))}$$

and for depths greater than d_c:

$$\frac{v_i}{V_{total}} = \frac{V_{top}}{V_{total}} * \frac{v_i}{V_{top}} = \frac{2 * \delta h}{d_c + 2 * (Z_o - d)c)}$$

From this we can then calculate the fraction of melt supplied from each depth interval for the depleted ($Frac^d$) and enriched ($Frac^e$) components:

$$Frac_i^d = \frac{Ur_i * \frac{v_i}{V_{total}} * F_i^d}{\sum Ur_i * \frac{v_i}{V_{total}} * F_i^d}$$

$$Frac_i^e = \frac{Ur_i * \frac{v_i}{V_{total}} * F_i^e}{\sum Ur_i * \frac{v_i}{V_{total}} * F_i^e}$$

where Ur_i represents the relative rate of mantle upwelling at the depth corresponding to point i, and is assumed to be constant at each depth (i.e. no lateral change in the rate of mantle upwelling). If $Ur_i = 1$ the no active upwelling is present and the rate of mantle upwelling is equal to that generated in response to plate spreading. F_i^d and F_i^e represent the fraction of melt produces at that pressure interval.

The final compositino of the melt is derived by multiplying the instantaneous compositions of the melt from each depth interval (C_i^d) with the fraction of melt derived from that depth:

$$C^f = P_d * \sum(C_i^d * Frac^d) + (1 - P_d) * \sum(C_i^e * Frac_i^e)$$

where P_d represents the total fraction of melt derived from the depleted mantel component and is calculated as:

$$P_d = \frac{\sum(Ur_i * \frac{v_i}{V_{total}} * F_i^d * X_d)}{\sum(Ur_i * \frac{v_i}{V_{total}} * F_i^e * (1 - X_d)) + \sum(Ur_i * \frac{v_i}{V_{total}} * F_i^d * X_d)}$$

where X_d is the mass fraction of depleted material in the mantle source.

1.3. Calculating the Fe-isotope composition of mantle melts

In addition to the trace-element composition of magmas derived from melting of a 2-component mantle, we also calculate the $\delta^{56}Fe$ composition of melts formed form a 2-component (pyroxenite-bearing) mantle using non-modal batch melting equations from Williams and Bizimis (2014). In addition, the $\delta^{56}Fe$ composition of melts formed during melting of a: (i) spinel peridotite; (ii) garnet peridotite (Afonso et al., 2008); and (iii) garnet pyroxenite are also calculated (Fig. 4 in the main text).

The $\delta^{56}Fe$ composition of the melt formed at each step was calculated using a mass balance approach where the $\delta^{56}Fe$ of each phase (including the melt) can be calculated if the proportions of each phase, concentration of FeO in each phase, and the isotopic fractionation factors between each phase are known. For simplicity we treat Fe as a trace-element so that is can be assigned partition coefficients during mantle melting. The partition coefficients chosen were those used in the calculations of Williams and Bizimis (2014) so that our results could be directly compared. At each pressure interval in our model theorectical Fe-O bond force constants for the 5 mantle mineral phases were calculated using the method of Sossi and O'Neill (2017). These force constants were sued to define mineral fractionation factors at each step (termed $\Delta^{56}Fe_{ol-min} = \delta^{56}Fe_{ol} - \delta^{56}Fe_{min}$) and melt-olivine fractionation factors ($\Delta^{56}Fe_{melt-ol} = \delta^{56}Fe_{melt} - \delta^{56}Fe_{ol}$) were calculated using the Fe-O force constants for basaltic melt that are estimated from NRIXS measurements by Dauphas et al. (2014).

Once these fractionation factors have been calculated the $\delta^{56}Fe$ composition of the melts formed at each pressure increment can be calculated using the following method:

For each component the $\delta^{56}Fe$ composition of the melt formed at each pressure interval can be calculated as:

$$\delta^{56}Fe_i^{d/e} = \frac{\delta^{56}Fe_{initial}^{d/e} * [Fe]_{initial}^{d/e} + \Delta^{56}Fe_{melt-ol} * \sum(n_i^{min} * [Fe]_i^{min}) + \sum(n_i^{min} * [Fe]_i^{min} * \Delta^{56}Fe_{ol-min})}{F_i * [Fe]_i^{melt} + \sum(n_i^{min} * [Fe]_i^{min})}$$

where n_i^{min} represents the proportion of that mineral phase int he system and F_i is the melt fraction at point i. At every depth in the model $F_i + \sum n_i^{min} = 1$, for both the enriched and depleted source components.

In addition, the concentration of Fe and $\delta^{56}Fe$ composition of the residue is calculated at each step:

$$\delta^{56}Fe_i^{res-d/e} = \frac{\delta^{56}Fe_{initial}^{d/e} * [Fe]_{initial}^{d/e} - F_i * \delta^{56}Fe_i^{d/e} * [Fe]_i^{d/e}}{(1 - F) * [Fe]_i^{res-d/e}}$$

These residue compositions are then used as the 'initial' $\delta^{56}Fe$ and $[Fe]$ for the next step in the model. Using this method we calculate the $\delta^{56}Fe$ composition of the instantaneous melts from 2-components during adiabatic upwelling. We can then use these results to calculate the $\delta^{56}Fe$ composition of the aggregated melt by:

Firstly, the aggregated $\delta^{56}Fe$ composition of melts from the enriched and depleted components are calculated seperately. For the depleted component the Fe-isotope composition and Fe concentration in the aggregated melt is:

$$\delta^{56}Fe^{d}_{final} = \frac{\sum([Fe]^{d}_{i} * \delta^{56}Fe^{d}_{i} * Frac^{d}_{i})}{\sum([Fe]^{d}_{i} * Frac^{d}_{i})}$$

$$[Fe]^{d}_{final} = \sum([Fe]^{d}_{i} * Frac^{d}_{i})$$

and for the enriched component:

$$\delta^{56}Fe^{e}_{final} = \frac{\sum([Fe]^{e}_{i} * \delta^{56}Fe^{e}_{i} * Frac^{e}_{i})}{\sum([Fe]^{e}_{i} * Frac^{e}_{i})}$$

$$[Fe]^{e}_{final} = \sum([Fe]^{e}_{i} * Frac^{e}_{i})$$

Using these results, we are then able to calculate the final $\delta^{56}Fe$ composition of the aggregated melt:

$$\delta^{56}Fe_{final} = \frac{P_d * [Fe]^{d}_{final} * \delta^{56}Fe^{d}_{final} + (1 - P_d) * [Fe]^{e}_{final} * \delta^{56}Fe^{e}_{final}}{P_d * [Fe]^{d}_{final} + (1 - P_d) * [Fe]^{e}_{final}}$$

This method is used to calculate the composition of melts formed via melting of a 2-component (peridotite-pyroxenite) mantle, as well as the individual melts formed during melting of 3 separate lithologies (Fig. 4 main text). Furthermore, we also use this method, coupled to pHMELTS mantle melting models to calculate the $\delta^{56}Fe$ composition of melts formed during adiabatic decompression melting beneath a ridge under different oxygen fugacity conditions (see below).

2. Fractional Crystallisation Correction

In order to compare along-ridge variations in the composition of melts delivered to the Galápagos Spreading Centre (GSC) it is necessary to correct for low-pressure crystallisation. In this study, the composition of all samples with MgO>5.5 wt% can be explained by crystallisation of clinopyroxene, plagioclase, and olivine from mantle derived melts. More evolved samples that have previously been analysed from the GSC (Christie et al., 2005) require fractionation of magnetite and we do not correct these samples for the influence of low-P crystallisation. However, it is clear from Fig S.1 that all samples from the GSC do not follow a single fractional crystallisation path, and therefore a single liquid-line-of-descent cannot be used to apply a fractional crystallisation correction to all samples. As a result, we have split the geochemical data from the GSC into three groups based on their La_n/Sm_n and K/Ti contents.

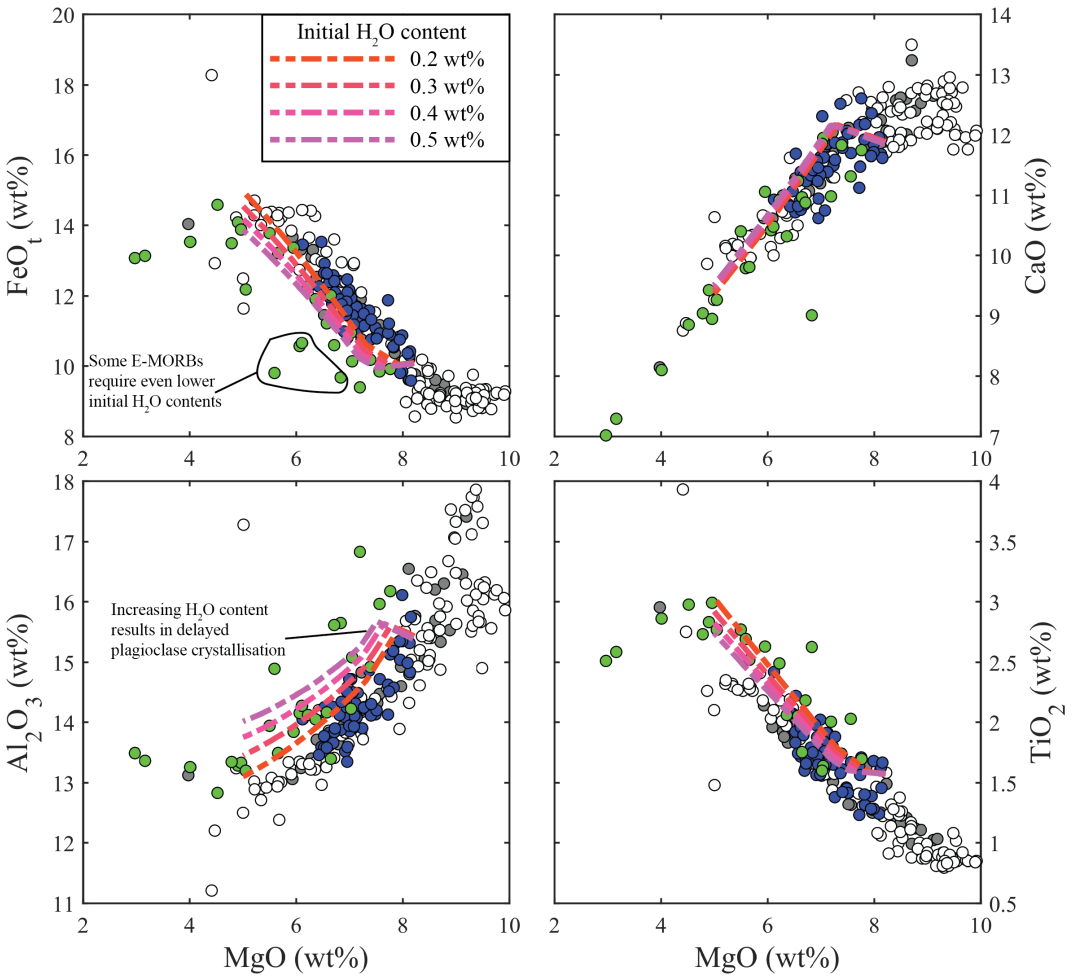

Fig S.1: *Compositional variation seen in the basaltic samples from the GSC. Colour scheme is the same as in the main text. Also shown are fractional crystallisation curves for a range of water contents using a set starting composition.*

The composition of these three groups is compared to a series of fractional crystallisation models run in Petrolog v3.1.1.3 (Danyshevky and Plechov, 2011) using a modified version of the least-squared based method of Gleeson et al. (2017). When the best fit fractional crystallisation model is found, the proportion of olivine, clinopyroxene, and plagioclase crystallising at each step is used to correct the major- and trace-element concentration of the GSC basalts for the influence of fractional crystallisation using partition coefficients from Kelemen et al. (2003) and Aigner-Torres et al. (2007).

Our method differs from that used by Gleeson et al. (2017) in that it considers the fit between the model and observed data at every point in that model run, whereas Gleeson et al. (2017) searched within a model for the single point that provided the best fit to all data points simultaneously. As a result, our new method is far better when considering geochemical trends, rather than trying to match a single point or tightly clustered group of data. The method used is described in detail below:

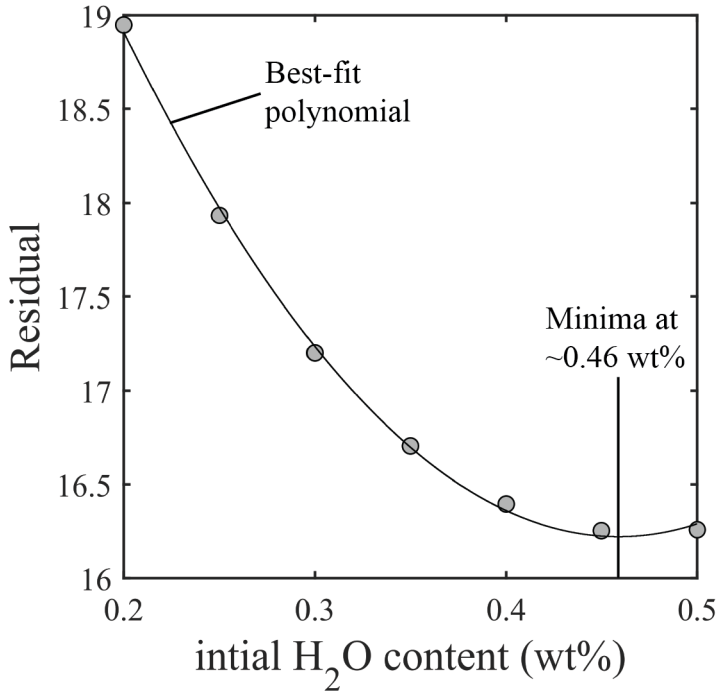

Fig S.2: *Minimum weighted residuals of the E-MORBs at various initial water contents. For all models show the pressure of crystallisation was kept constant at 100 MPa. It can be seen that a minimum in the residual curve occurs at 0.46 wt% H_2O showing that the E-MORBs are characterised by much higher volatile contents than the N-MORBs and D-MORBs.*

1. Best fit polynomial curves (2nd order) are calculated for each element under consideration vs MgO content.
2. The distance between the polynomial curve and the actual data is calculated at the MgO content of each data point.
3. The apparent standard deviation of the data (i.e. scatter around the best fit polynomial) is then calculated using these residuals. For MgO the apparent standard deviation is calculated as the 2σ analytical uncertainty in our EPMA analysis.
4. The minimum weighted residual of each model is then calculated by:
   (a) Calculating the residual between the model and a single data point (i) at every point along the modelled liquid-line-of-descent (j).

$$R_i^j = \sum_{k=1}^{n} \frac{(X_i^k - \hat{X_j^k})^2}{X_{sd}^k}$$

   Where X_i is the concentration of oxide X in the data point under consideration; $\hat{X}_j$ is the concentration of the same oxide in the model at point j; and X_{sd} is the apparent standard deviation of that oxide around its polynomial regression. The value of k denotes which oxide is under consideration at each point, and is used to show that this equation is summed over all oxides considered for every model data point.
   (b) This produces a 2-dimensional matrix where each column represents a single sample (i), and each row represents the residual between the model and that sample at each step of the model. We therefore search through each

row to determine the closest match of each model to each individual datapoint (i.e. the minimum value of each row). This results is a single column vector containing a 'minimum residual' value for each sample under consideration termed Rm_i.

(c) The sum of Rm_i is then calculated to provided the minimum weighted residual of each model (Fig S.2).

3. Major-element systematics of the Santiago basalts

Beneath Isla Santiago in the Central Galapagos the lithological properties of the mantle source are uncertain. Gleeson and Gibson (2019) recently showed that the low-K tholeiitic basalts from this region are derived from a peridotitic source, but some evidence (from olivine chemistry) indicates that a pyroxenitic component may exist in the region (Vidito et al., 2013). However, as high MgO basalts (∼8-9 wt%) have been found on western Santiago, careful consideration of the major-element systematics and olivine chemistry of these basalts can be used to investigate the lithological nature of the mantle source region in this region.

The mildly alkaline basalts from western Santiago are characterised by elevated FeO_t and TiO_2 as well as lower CaO and Al_2O_3 that the tholeiitic basalts of eastern Santiago, which have been shown to originate from a peridotitic source (Gleeson and Gibson, 2019; Gibson et al., 2012). Comparison of the major-element systematics of these different geochemical groups to melting experiments carried out on a range of source lithologies (following the method of Shorttle and Maclennan, 2011) indicates that tholeiitic basalts of eastern Santiago are best matched by melting of peridotite source lithologies (KLB-1; Hirose, 1993) as expected, whereas the mildly alkaline basalts of western Santiago are matched by melting of a pyroxenite source (e.g. M5-40; Lambart et al., 2013; Fig S.3). These results indicate that a significant contribution of melts from a pyroxenitic source is present in the mildly alkaline basalts of western Santiago.

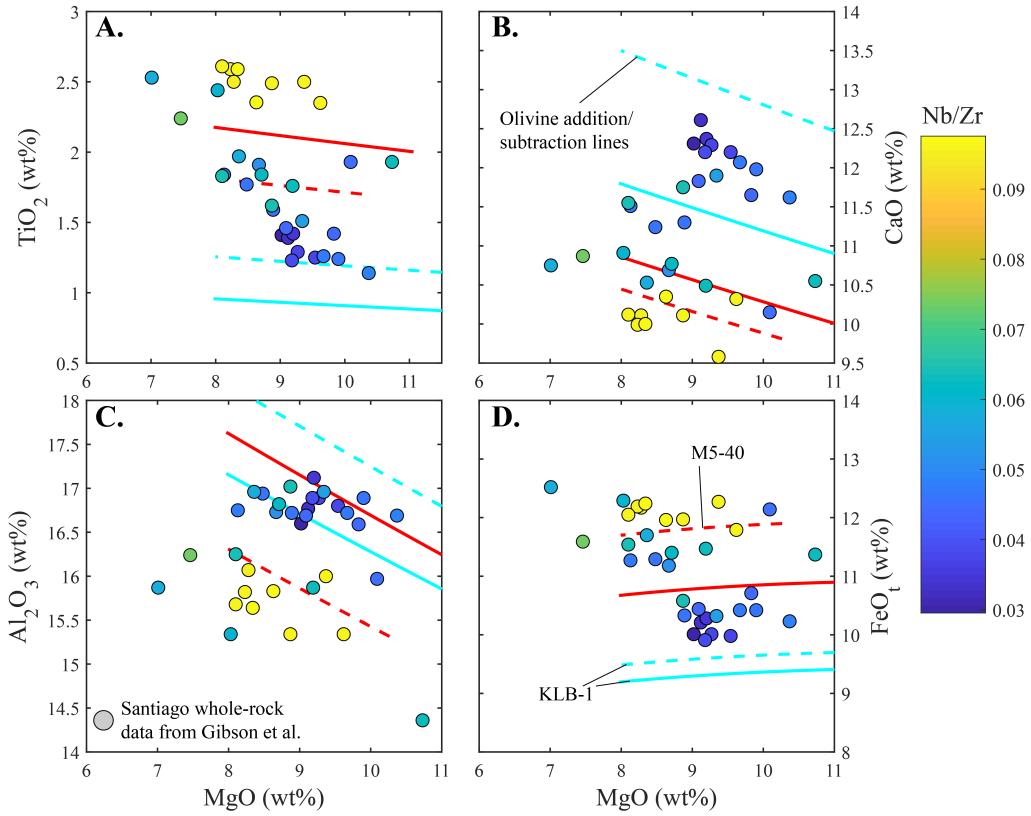

Fig S.3: *Results of major-element analysis on the Santiago basalts by Gibson et al. (2012) are compared to compositions predicted by melting experiments on different lithologies. The composition of mildly-alkaline basalts from western Santiago (which generally possess high Nb/Zr ratios) are best reproduced using a pyroxenitic source component (M5-40) from Lambart et al. (2013).*

4. Influence of changing model parameters

4.1. Choice of pyroxenite starting composition

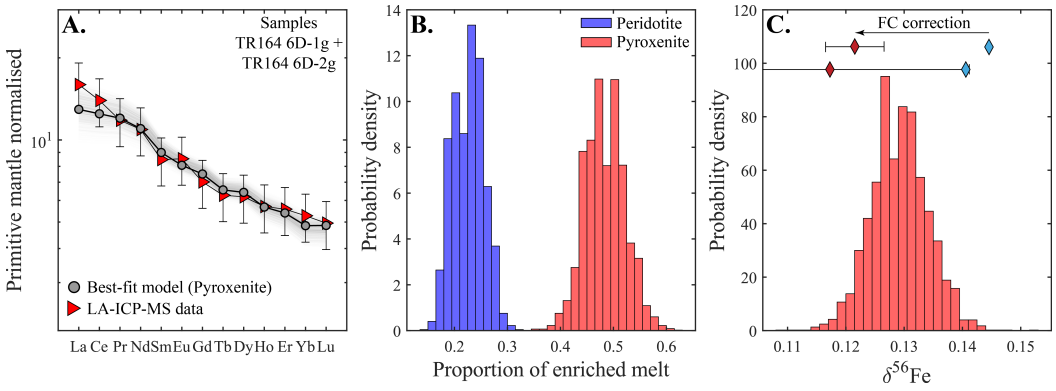

Fig S.4: *This figure represents a replicate of Fig. 4 in the main text. However, in this case the major-element composition of the pyroxenitic end-member is set as pyroxenite M7-16 rather than M5-40 (Lambart et al., 2016). When this pyroxenite is used the proportion of melt derived from this component that is required to explain the composition of samples TR164 6D-1g and TR164 6D-2g is far higher than if pyroxenite M5-40 is used. As a result, the Fe-isotope composition of the pyroxenitic end-member does not need to be as heavy as suggested in the main text. Panel* ***C.*** *shows the predicted Fe-isotope composition of these samples assuming a peridotite end-member with a* δ^{56}*Fe composition of* $+0.01$‰ *and a pyroxenitic end-member with a* δ^{56} *composition of* $+0.08$‰.

4.2. Analysis repeated with the two most enriched samples removed from consideration

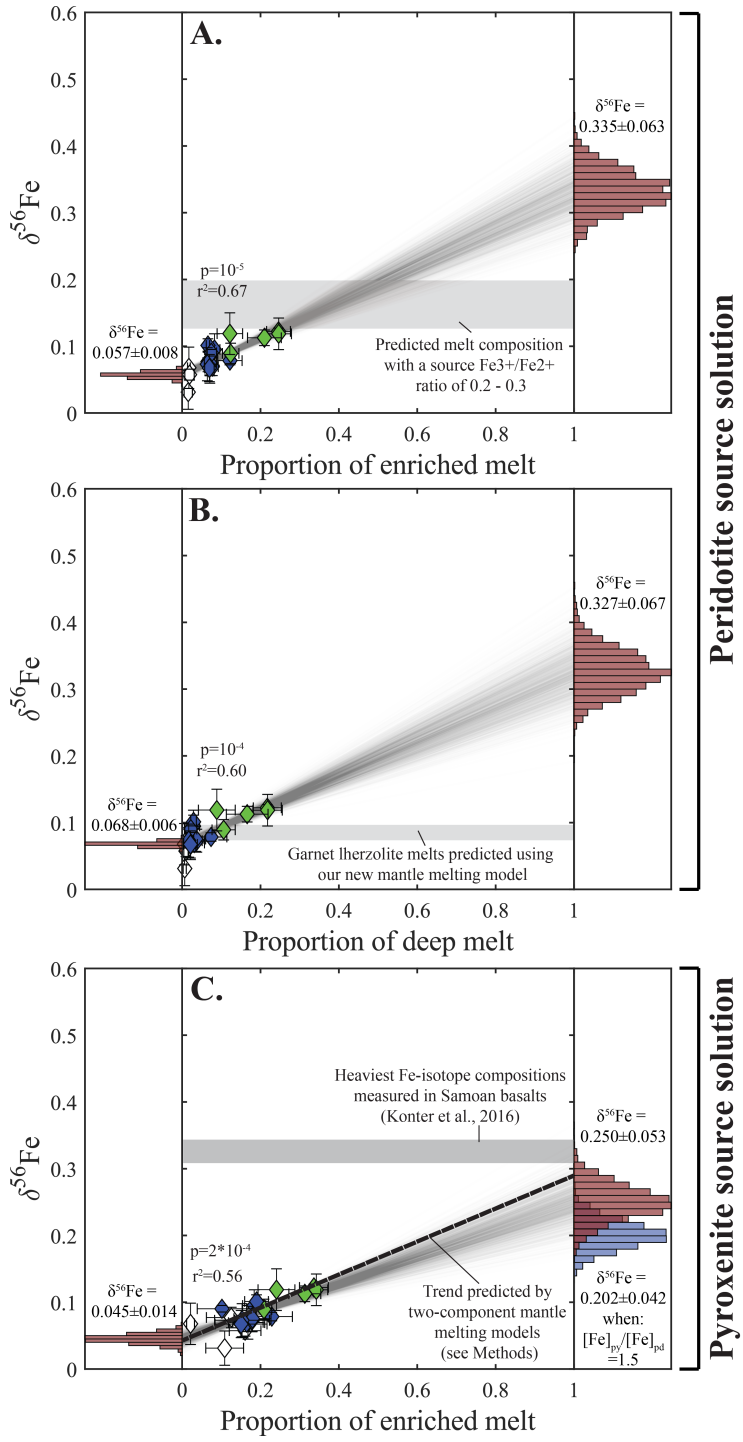

Fig S.5: *Shown is a replicate of Fig. 5 from the main text, but in this case the two most enriched samples from the GSC are excluded. It can be seen that the arguments presented in the main text are still supported by our analysis even if these anomalous samples are removed from consideration.*

4.3. Influence of fractionation factors chosen for fractional crystallisation correction

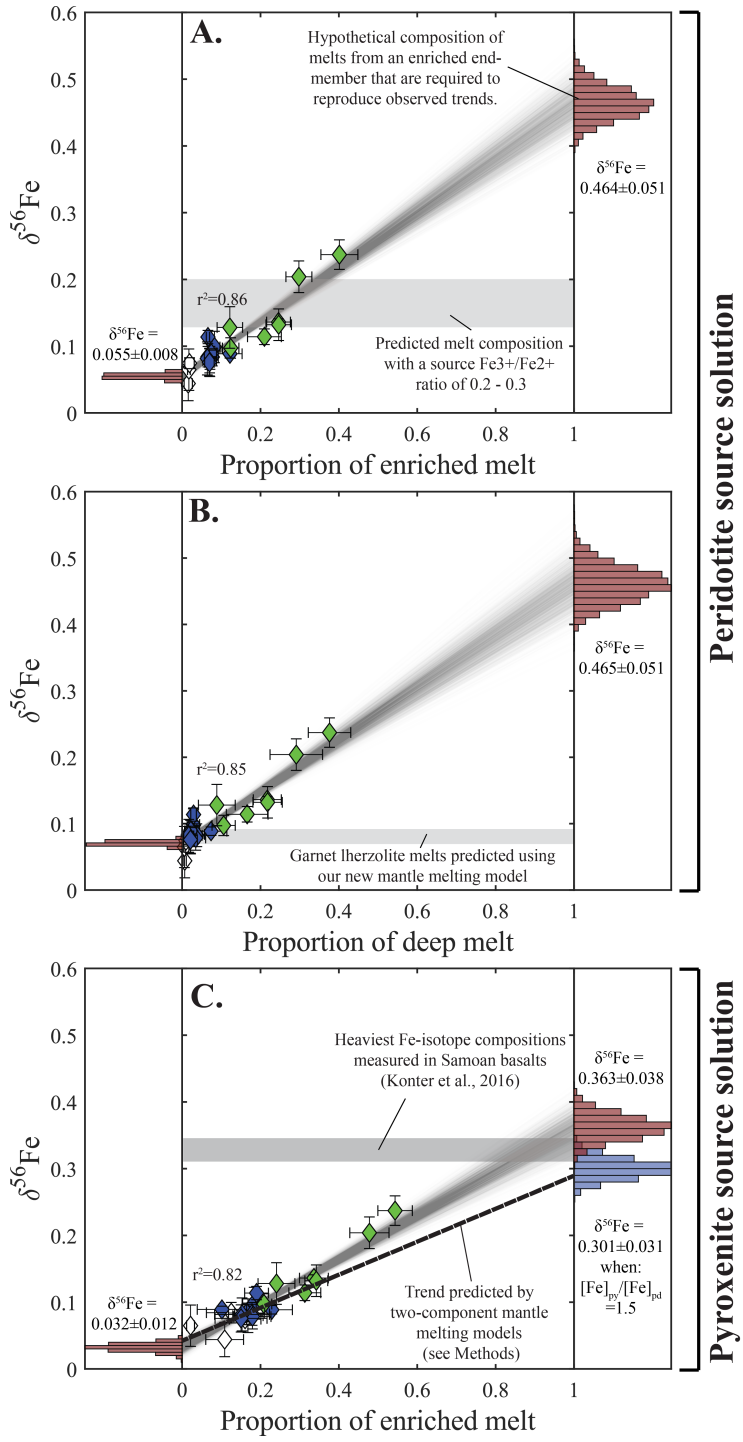

Fig S.6: *Shown is a replicate of Fig. 5 from the main text, but in this case the fractional crystallisation correction is carried out using fractionation factors calculated from Fe-O bond force constants from Dauphas et al. (2014).*

5. Calculating the extent of Fe-isotope fractionation during mantle melting

5.1. Influence of isotopically-light garnet

In addition to calculating the Fe-isotope composition of melts formed during adiabatic decompression melting of a 2-component mantle using melting equations for a spinel peridotite and garnet pyroxenite (see Methods), we also calculate the composition of melts formed during fractional melting of a garnet lherzolite (Table S.1). Mineral-olivine and olivine-melt fractionation factors are calculated in the same way as described in the main text, and the starting peridotite was assumed to have a $\delta^{56}Fe$ composition of $+0.025‰$. The results of this analysis are shown in Fig. S.7, and indicate that although the predicted Fe-isotope fractionation is slightly larger for a garnet lherzolite that for a spinel lherzolite, the extent of Fe-isotope fractionation is not enough to explain the Fe-isotope heterogeneity observed in the GSC basalts. Melt modes for a garnet lherzolite is taken from Afonso et al. (2008).

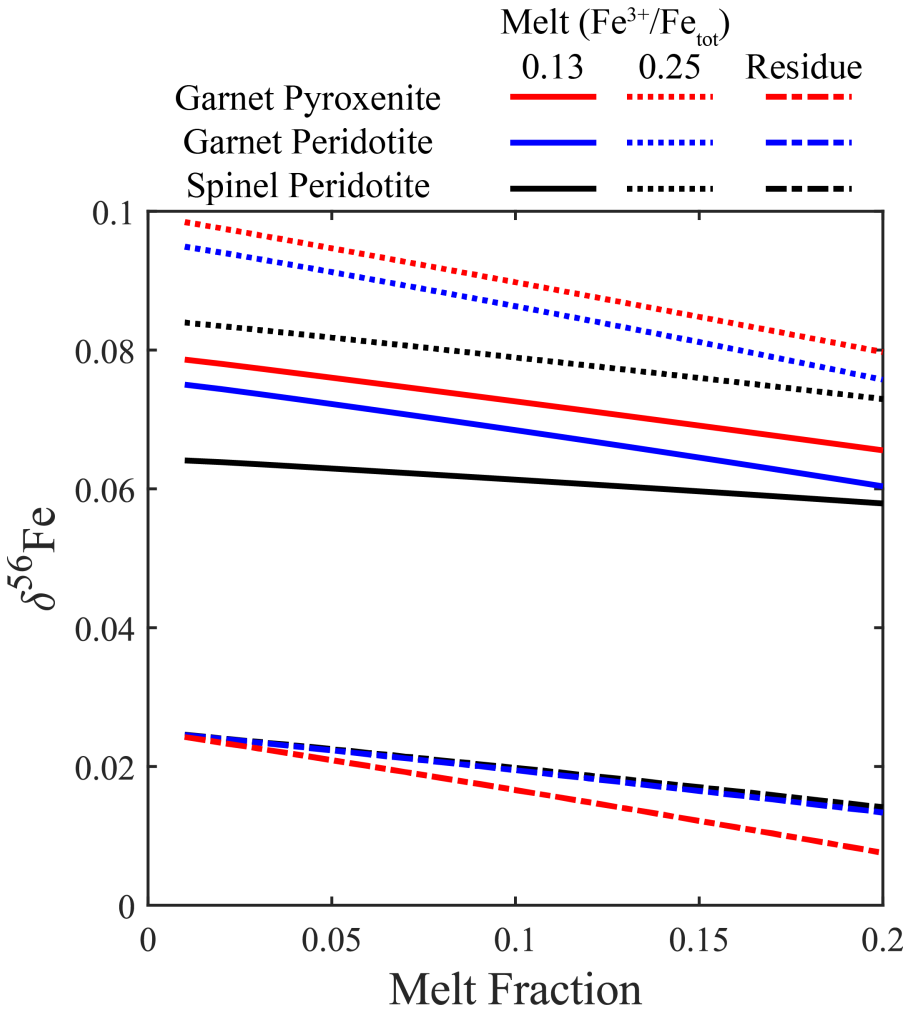

Fig S.7: *Fe-isotope composition predicted during fractional melting of a. Garnet peridotite; b. spinel peridotite; and c. garnet pyroxenite. It can be seen that melts of a garnet pyroxenite are predicted to be marginally heavier than those of a spinel peridotite, but this variation is not large enough to explain the heterogeneity in the composition of the GSC basalts.*

5.2. Influence of oxygen fugacity

The maximum influence that oxygen fugacity may play on the $\delta^{56}Fe$ composition of the GSC basalts is investigated using the model of Dauphas et al. (2009). In this model Fe^{3+} is treated as more strongly incompatible than Fe^{2+} during mantle melting ($D_{Fe^{3+}} = 10$; $D_{Fe^{2+}} = 1$). In addition, there is an isotopic fractionation that is assumed to occur between Fe^{3+} and Fe^{2+} such that $\delta^{56}Fe^{3+} - \delta^{56}Fe^{2+} = +0.3‰$. Using the model of Dauphas et al. (2009) we tested the influence of changing the source Fe^{3+}/Fe^{2+} ratio on the Fe-isotope composition of the melt. Results indicate that the maximum $\delta^{56}Fe$ composition of basaltic melt that can be achieved by changing the oxygen fugacity of the source is approximately $+0.18‰$. This is far lower than is required to explain the heterogeneity observed in the GSC basalts.

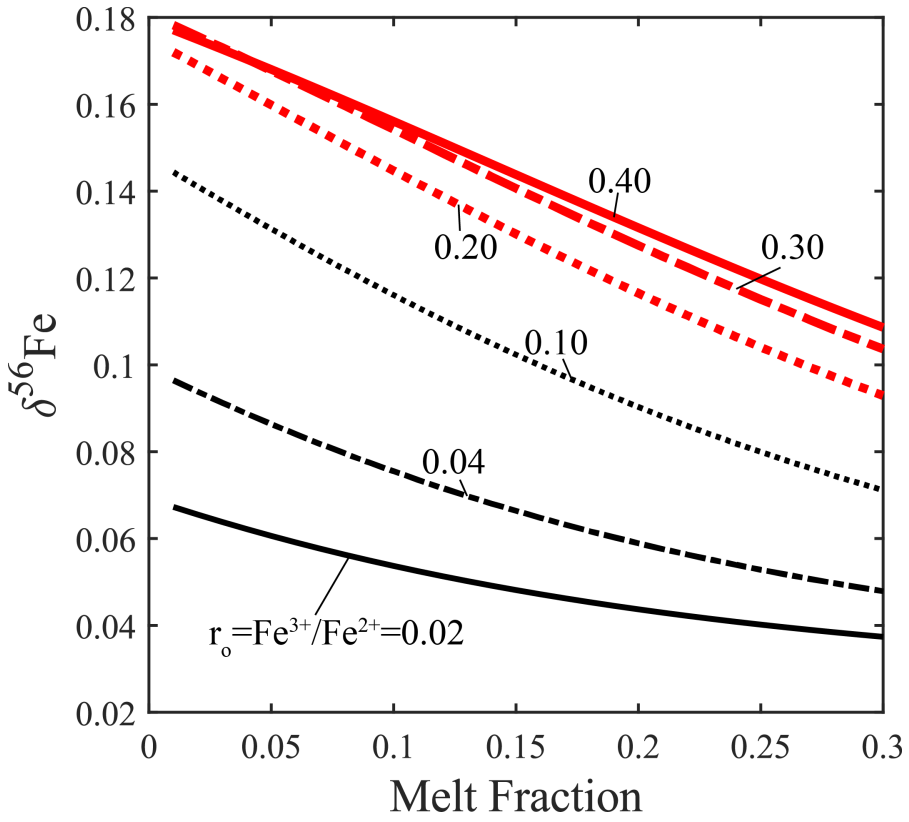

Fig S.8: *Fe-isotope composition of melts predicted from sources that have varying initial ferric - ferrous Fe ratios according to the model of Dauphas et al. (2009).*

5.3. Full thermodynamic consideration of Fe-isotope fractionation during mantle melting

In addition to the simple models for melting of: (i) spinel lherzolite; (ii) garnet lherzolite; and (iii) garnet pyroxenite shown above (and in the main text), we consider the Fe-isotope fractionation that may result from adiabatic decompression melting of a peridotitic mantle beneath a Mid-Ocean Ridge. This is carried out using alphaMELTS to calculate the partitioning of Fe between all phases that are present at each pressure interval during fractional melting. In addition, we use alphaMELTS to constrain the ratio between ferric and ferrous Fe in each phase at every pressure increment and use this data to calculate Fe-O force constants and Olivine-X fractionation factors (where X represents either basaltic melt or another mineral phase) using the methods of Sossi and O'Neill (2017); Macris et al. (2015); and Dauphas et al. (2014).

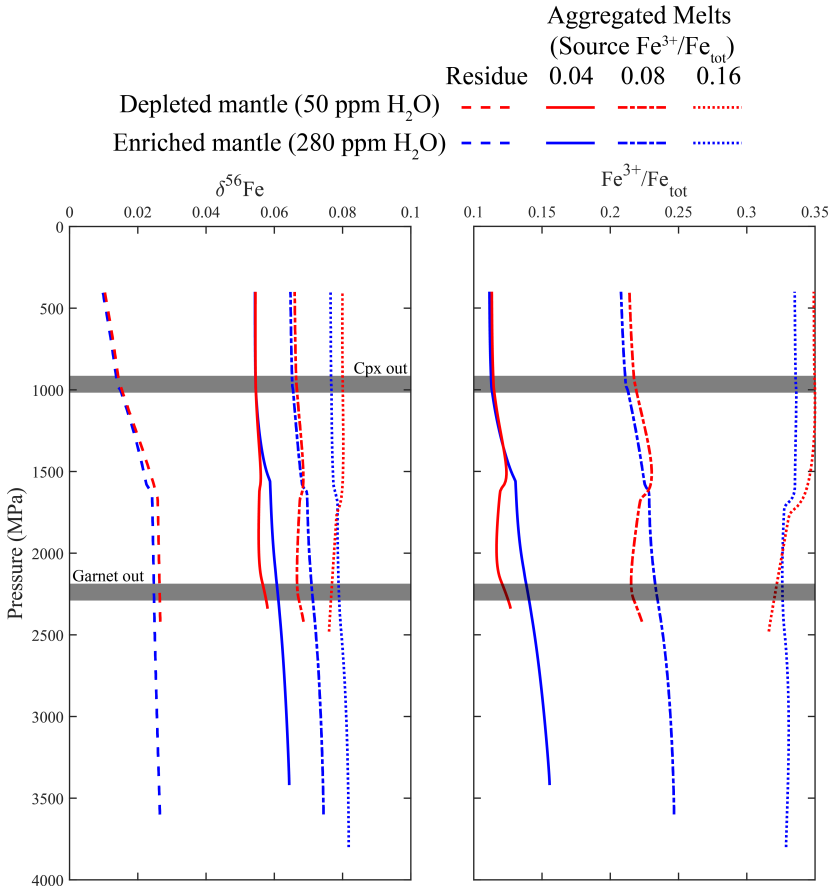

Fig S.9: *Graphs showing* ***A.*** *the* $\delta^{56}Fe$ *and* ***B.*** Fe^{3+}/Fe_{tot} *content of aggregated mantle melts in a 2-D melting regime beneath a Mid-Oceanic Ridge. These graphs show that even very large variations in the redox state of the mantle* ($Fe^{3+}/Fe_{tot} = 0.04 - 0.16$) *cause only minor changes in the* $\delta^{56}Fe$ *composition of the aggregated mantle melts. As a result we do not currently have the analytical precision required to identify variations in* fO_2 *based on variations in the* $\delta^{56}Fe$ *composition of basaltic melts. In addition, there is no clear difference in the composition of aggregated melts derived from the garnet stability field compared to those derived purely from the spinel stability field.*

Results of this analysis indicate that variations in the fO_2 of the mantle source, and also the influence of deep melting in the garnet stability field, cannot cause a large enough variation in the $\delta^{56}Fe$ composition of primary mantle melts to explain the heterogeneity

observed in the GSC basalts. As a result significant heterogeneity in the Fe-isotope composition of the mantle source is required in order to explain our data.

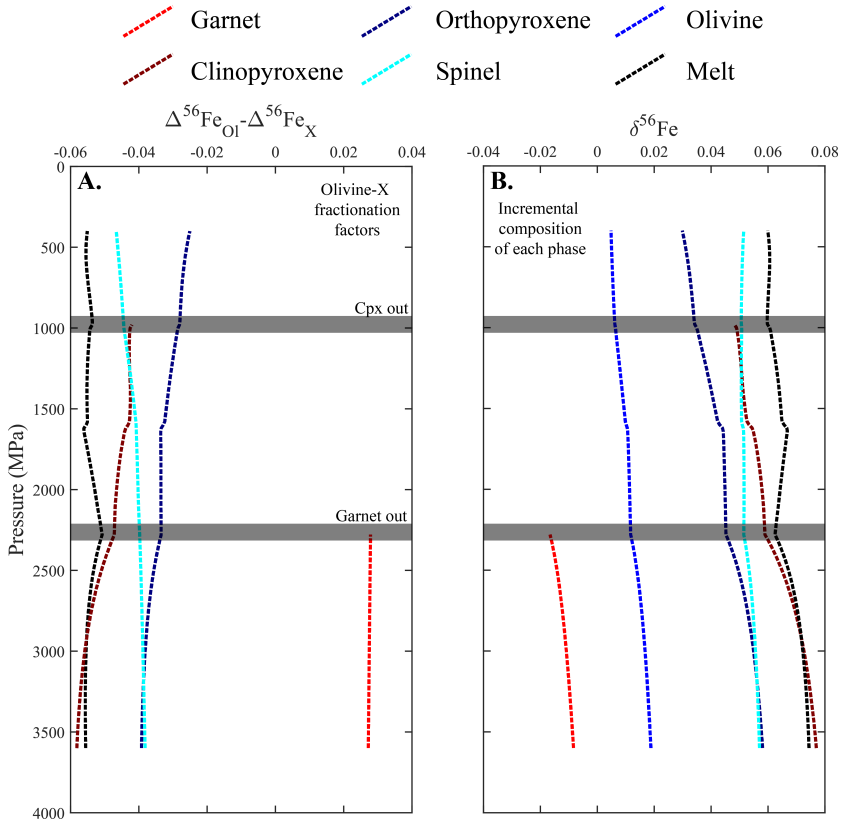

Fig S.10: ***A.*** *Olivine-X fractionation factors, and* ***B.*** *incremental $\delta^{56}Fe$ composition of each phase. Fractionation factors are calculated using the method of Sossi and O'Neill (2017) and the Fe-O force constant of the melt phase is calculated using the NRIXS data from Dauphas et al. (2014). The models shown are for a mantle source with a H_2O content of 280 ppm and a Fe^{3+}/Fe_{tot} ratio of 0.08.*

6. Results of mantle melting models

The following two figures show the results of mantle melting models for samples TR164 6D-1g and TR164 6D-2g for a peridotite and and pyroxenite source.

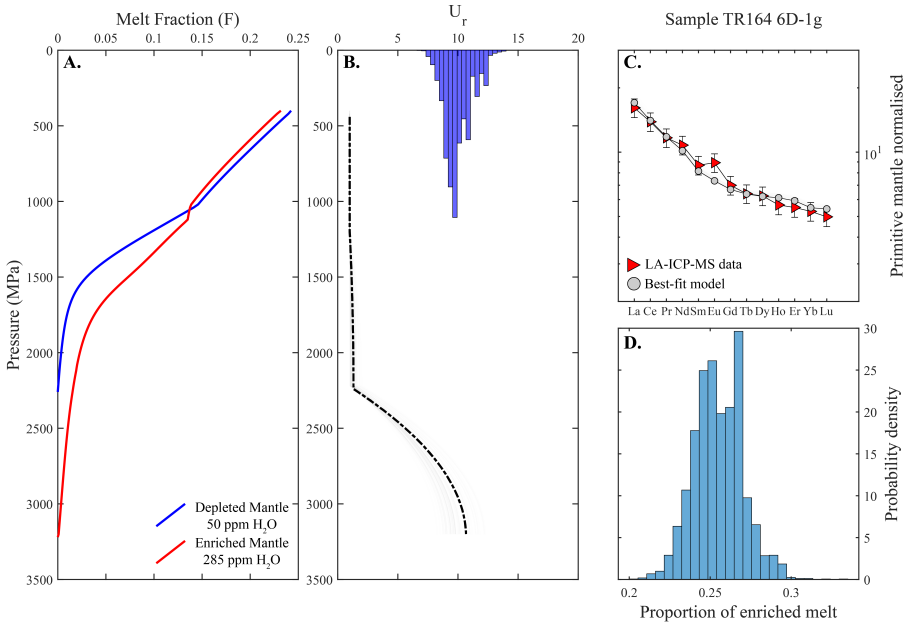

Fig S.11: *Results of our mantle melting models (for a 2-component peridotitic mantle). Panel* ***A.*** *shows the melt fraction vs depth curves for an anhydrous (50 ppm H_2O) and relatively hydrous (∼285 ppm $H)2O$) peridotite. Panel* ***B.*** *shows the relative upwelling velocity profile beneath the ridge. The dashed black line represents the best fit model to the REE composition of sample TR164 6D-1g. The REE composition predicted by this model is compared to the empirical data from sample TR164 6D-1g in panel* ***C.****. Probability density distribution for the proportion of enriched melt that contributes to this sample is show in panel* ***B.****.*

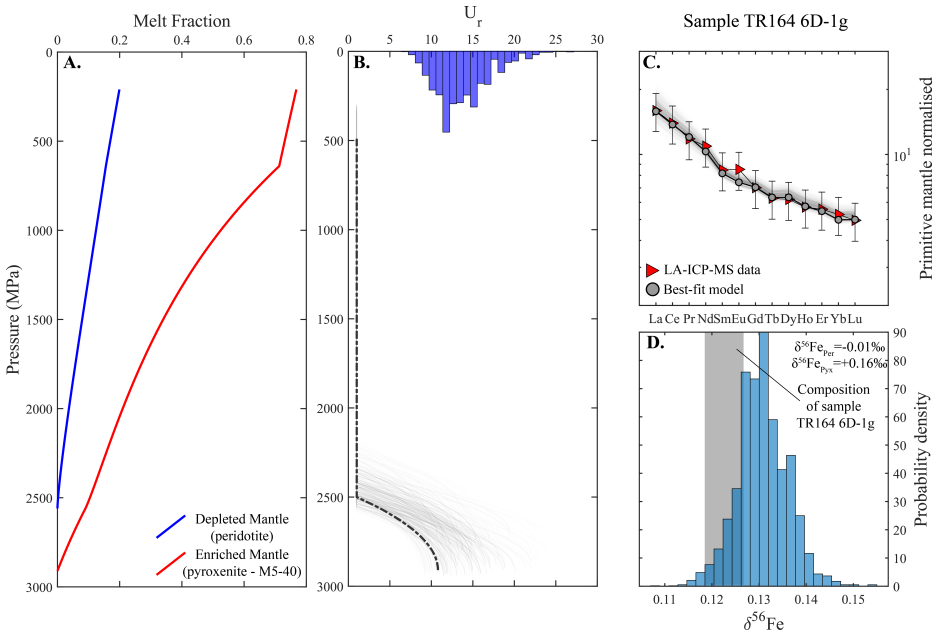

Fig S.12: *Results of our mantle melting models for a 2-component mantle containing an isotopically enriched component. The melt-fraction vs depth curves for the peridotite and pyroxenite components are calculated following the method of Lambart et al. (2016). Similarly to Fig. S.9. The black line in panel* ***B.*** *and grey symbols in panel* ***C.*** *represent the best fit solution to the empirical data collected for sample TR164 6D-1g by LA-ICP-MS. The $\delta^{56}Fe$ composition of the melt that is predicted by our mantle melting model is shown in panel* ***D.****. It can be seen that the $\delta^{56}Fe$ value predicted by these model very slightly overpredict the $\delta^{56}Fe$ composition of sample TR164 6D-1g, the $\delta^{56}Fe$ composition of the starting materials in this model were chosen in order to provide the best possible match to all samples simultaneously.*

7. Optimisation of LA-ICP-MS analysis of basaltic glass

Systematic testing of basaltic glass analysis by the new 193 laser-ablation ICP-MS system at the University of Cambridge was required in order to optimise analytical conditions. We carried out systematic tests on spot size, fluence, and repetition rate. Matrix effects were also investigated by varying the calibration material between NIST SRM 612 and BCR-2G standard glasses, but similar results were observed in both cases. Results are presented for a range of trace-elements including rare earth elements (REE), first row transition elements (FRTE), large ion lithophile elements (LILE), and high field strength elements (HFSE).

A similar study on the accuracy and precision of LA-ICP-MS analysis was carried out by Jenner and O'Neill (2012). Their study determined that a precision of ¡4% can commonly be achieved for a suite of 20 elements, when the 'optimal ablation diameter' is used. The precision and accuracy of analysis depends on a number of variables, including the ablation diameter, laser repetition rate and fluence, and other factors kept constant in this analysis (e.g. ablation time, counting times per element; choice of internal and external standard materials Jackson et al., 1992). Counting statistics, dependent on how much material is bought into the ICP-MS, and matrix effects during ablation both control the accuracy and precision of analysis (Jenner and O'Neill, 2012).

7.1. Spot size

In order to test the effects of spot size we varied the ablation diameter from 30 to 140 μm at a constant fluence ($8J/cm^2$) and repetition rate (10 Hz). Results for the full suite of REE in BHVO-2G are shown in Fig. S.13. These results reveal that (for most REE) a RSD of $< 5\%$ can commonly be achieved when the ablation diameter is $> 60\mu m$. Below this value the precision of analysis rapidly decreases (precision of LREE $< 10\%$ and HREE $< 20\%$ at an ablation diameter of $40\mu m$). A similar effect occurs when the FRTE, LILE, and HFSE, are considered although the decrease in precision is not nearly as dramatic for the FRTE as it is for the REE. The accuracy of analysis is also dependent on the ablation diameter, and recovery is shown to fall closest to 1 in the range $60 - 100\mu m$ regardless of calibration material used. Overall, we conclude that the best precision and accuracy of analysis is achieved when the ablation diameter is between 80 and $100\mu m$ regardless of calibration material. The drop off in precision occurs at $\sim 60\mu m$ for enriched material (i.e. BHVO-2G) but at slightly larger ablation diameters for more depleted material (i.e. BIR-1G).

7.2. Fluence

Next we tested the effect of fluence (J/cm^2) on the precision and accuracy of our results. Fluence of $3 - 13.19J/cm^2$ were investigated. Similarly to ablation diameter, precision is shown to decrease at low fluence. At $> 6J/cm^2$ the precision of all REE and FRTEs are commonly $< 6\%$ and usually $< 4\%$, but this increases slightly at lower fluence ($< 14\%$ at $4J/cm^2$; Fig. S.14). Accuracy is near 100% for analysis at $8 - 10J/cm^2$ regardless of calibration material used. These results relate to REE, HFSE, LILE, and FRTE in both depleted and enriched samples (BIR-1G and BHVO-2G) and we therefore conclude that a fluence of $8 - 10J/cm^2$ represents the optimal analytical conditions. Whilst lower residuals are sometimes seen at higher fluence ($12 - 13.19J/cm^2$), variations in the ablation characteristics between the calibration material NIST SRM 612 and the unknown glass materials cause a decrease in the accuracy of the results.

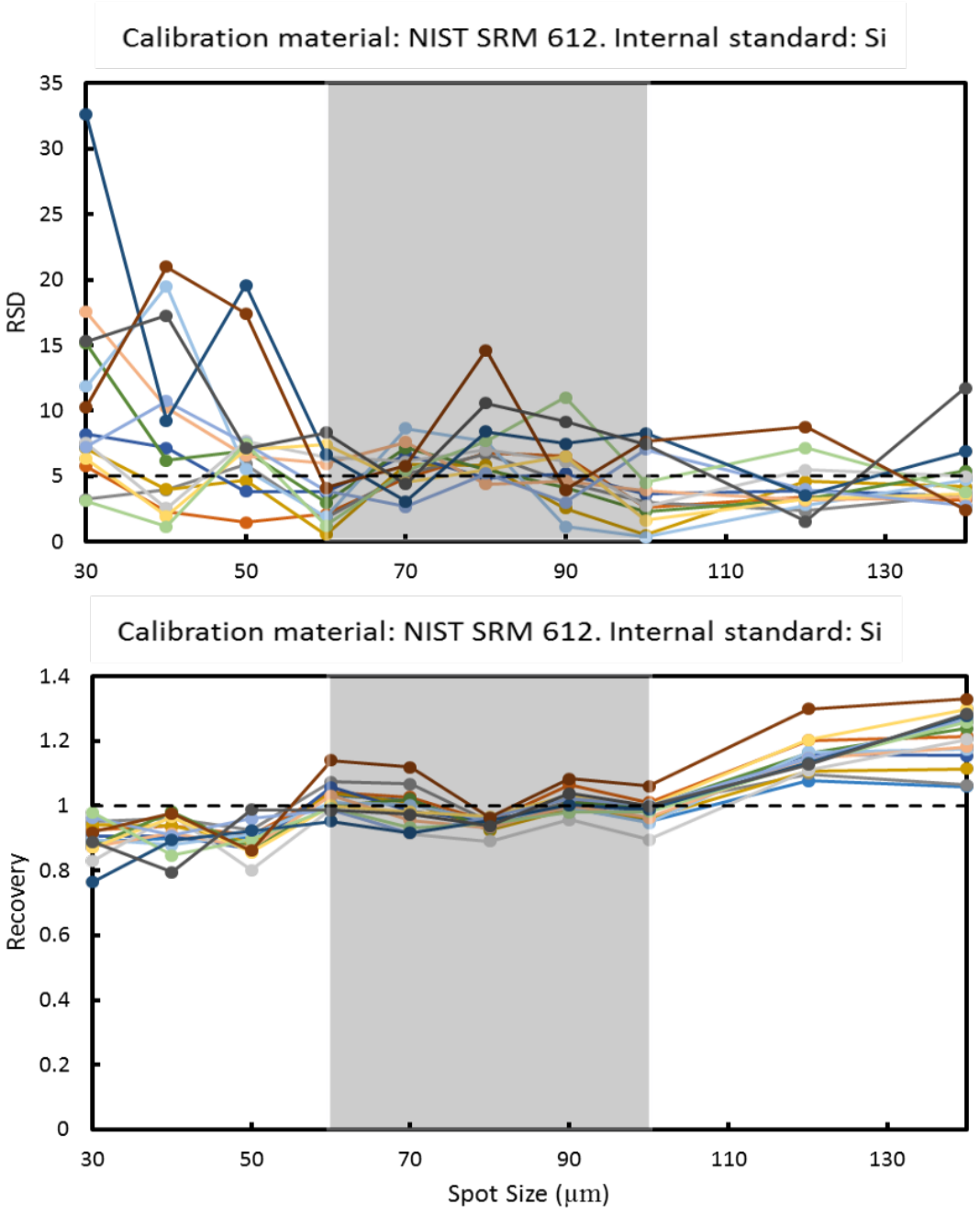

Fig S.13: *Precision and accuracy of REE analysis of BHVO-2G secondary standard material using different ablation diameters. Generally the best precision and accuracy is shown to be between 60 and 100 μm. Similar results are obtained for analysis of the more depleted BIR-1G glass standard. Shaded area indicates region of highest accuracy and precision. For all analysis shown here a Fluence of* $8J/cm^2$ *and a Repition Rate of* $10Hz$ *were used.*

7.3. Repetition rate

We varied the repetition rate between 5 and 20 Hz whilst using a fluence of $8J/cm^2$ and ablation diameter of $100\mu m$. The precision of analysis is observed to decrease with repetition rate, and the lowest RSD values are generally achieved at 20 Hz, although a precision of $< 6\%$ is seen for most elements at a repletion rate of 10 Hz (Fig. S.15). An accuracy of near 100% is achieved at a repetition rate of 10-20 Hz, but the concentration

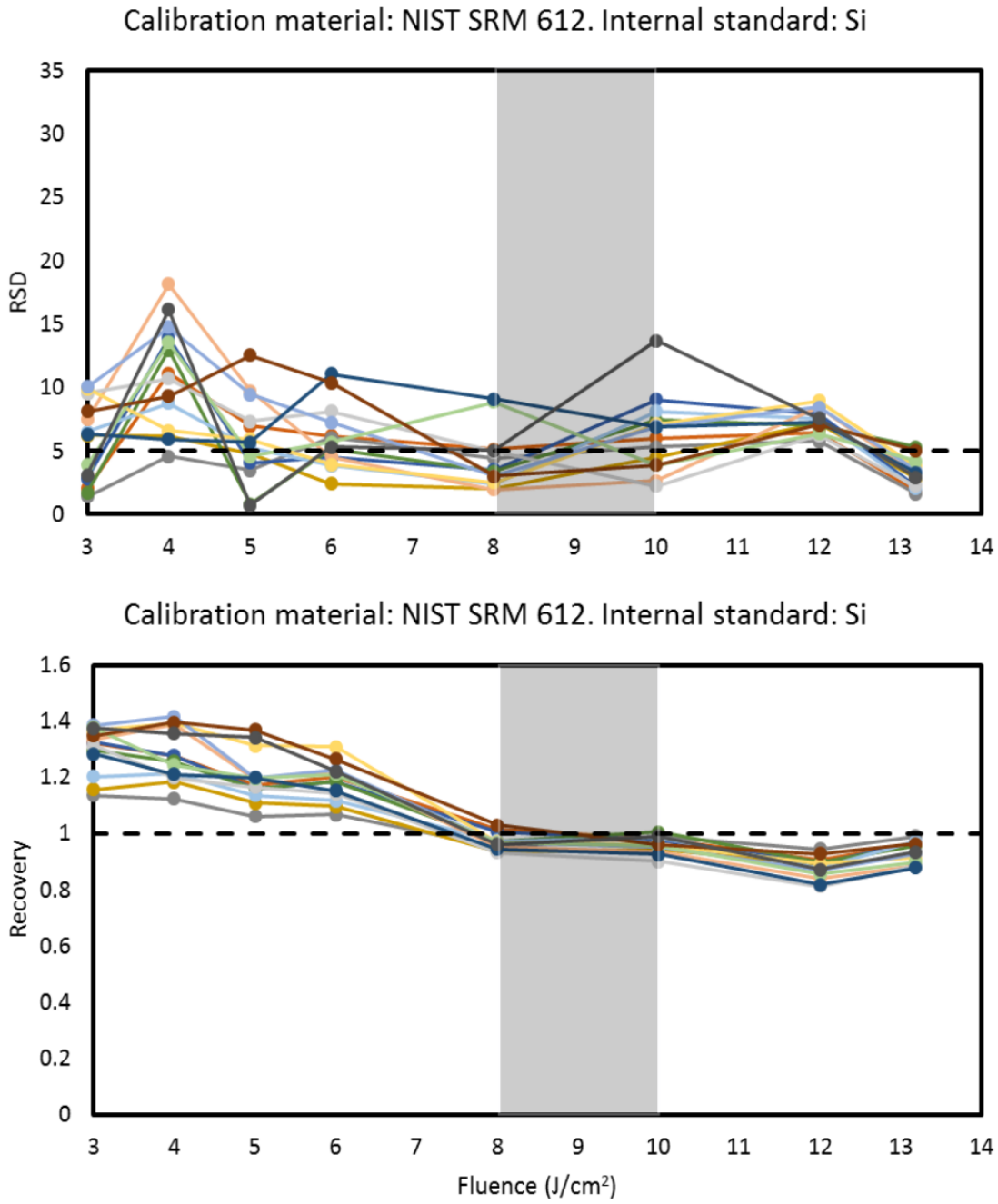

Fig S.14: *Precision and accuracy determined for analysis of REE in a BHVO-2G glass standard using different fluences. The best precision is seen at* $> 6J/cm^2$*, whereas the best accuracy is seen between* 8 *and* $10J/cm^2$*. Grey shaded area shows the conditions that give the highest accuracy and precision.*

of REE in the unknown material is over predicted at lower repetition rates. We therefore suggest that a repetition rate of 10-20 Hz should be used for analysis of basaltic glass.

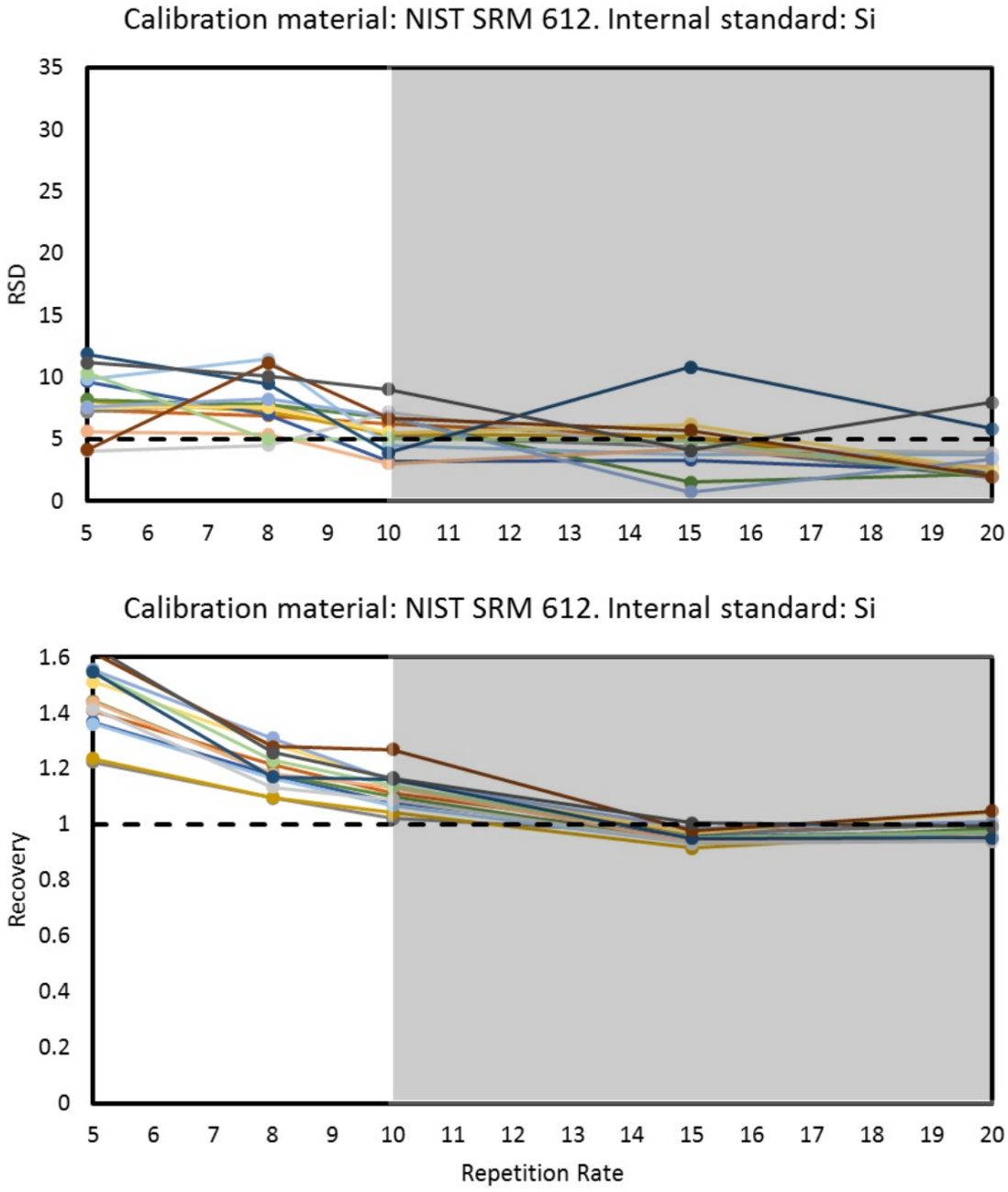

Fig S.15: *Precision and accuracy of analysis for REE in a BHVO-2G glass standard when different repetition rates (Hz) are used. Results suggest that below 10 Hz, the accuracy and precision of analysis is severely affected. Grey shaded area represents the conditions which give the best accuracy and precision.*

8. Additional references

Afonso, J.C., Fernandez, M., Ranalli, G., Griffin, W.L. and Connolly, J.A.D., 2008. Integrated geophysical-petrological modeling of the lithosphere and sublithospheric upper mantle: Methodology and applications. Geochemistry, Geophysics, Geosystems, 9(5).

Aigner-Torres, M., Blundy, J., Ulmer, P., Pettke, T., 2007. Laser Ablation ICPMS study of trace element partitioning between plagioclase and basaltic melts: an experimental approach. Contrib. Mineral. Petrol. 153, 647–667. https://doi.org/10.1007/s00410-006-0168-2

Christie, D.M., Werner, R., Hauff, F., Hoernle, K. and Hanan, B.B., 2005. Morphological and geochemical variations along the eastern Galápagos Spreading Center. Geochemistry, Geophysics, Geosystems, 6(1).

Danyushevsky, L.V. and Plechov, P., 2011. Petrolog3: Integrated software for modeling crystallization processes. Geochemistry, Geophysics, Geosystems, 12(7).

Dauphas, N., Craddock, P.R., Asimow, P.D., Bennett, V.C., Nutman, A.P. and Ohnenstetter, D., 2009. Iron isotopes may reveal the redox conditions of mantle melting from Archean to Present. Earth and Planetary Science Letters, 288(1-2), pp.255-267.

Dauphas, N., Roskosz, M., Alp, E.E., Neuville, D.R., Hu, M.Y., Sio, C.K., Tissot, F.L.H., Zhao, J., Tissandier, L., Médard, E. and Cordier, C., 2014. Magma redox and structural controls on iron isotope variations in Earth's mantle and crust. Earth and Planetary Science Letters, 398, pp.127-140.

Gleeson, M.L. and Gibson, S.A., 2019. Crustal controls on apparent mantle pyroxenite signals in ocean-island basalts. Geology, 47(4), pp.321-324.

Gleeson, M.L., Stock, M.J., Pyle, D.M., Mather, T.A., Hutchison, W., Yirgu, G. and Wade, J., 2017. Constraining magma storage conditions at a restless volcano in the Main Ethiopian Rift using phase equilibria models. Journal of Volcanology and Geothermal Research, 337, pp.44-61.

Gibson, S.A., Geist, D.G., Day, J.A. and Dale, C.W., 2012. Short wavelength heterogeneity in the Galápagos plume: Evidence from compositionally diverse basalts on Isla Santiago. Geochemistry, Geophysics, Geosystems, 13(9).

Hirose, K., 1997. Melting experiments on lherzolite KLB-1 under hydrous conditions and generation of high-magnesian andesitic melts. Geology, 25(1), pp.42-44.

Jackson, S.E., Longerich, H.P., Dunning, G.R. and Freyer, B.J., 1992. The application of laser-ablation microprobe; inductively coupled plasma-mass spectrometry (LAM-ICP-MS) to in situ trace-element determinations in minerals. The Canadian Mineralogist, 30(4), pp.1049-1064.

Jenner, F.E. and O'Neill, H.S.C., 2012. Major and trace analysis of basaltic glasses by laser-ablation ICP-MS. Geochemistry, Geophysics, Geosystems, 13(3).

Kelemen, P.B., Yogodzinski, G.M., Scholl, D.W., 2003. Along-strike variation in the Aleutian Island Arc: Genesis of high Mg# andesite and implications for continental crust, in: Eiler, J. (Ed.), Geophysical Monograph Series. American Geophysical Union, Washington, D. C., pp. 223–276. https://doi.org/10.1029/138GM11

Konter, J.G., Pietruszka, A.J., Hanan, B.B., Finlayson, V.A., Craddock, P.R., Jackson, M.G. and Dauphas, N., 2016. Unusual $\delta^{56}Fe$ values in Samoan rejuvenated lavas generated in the mantle. Earth and Planetary Science Letters, 450, pp.221-232.

Lambart, S., Laporte, D. and Schiano, P., 2013. Markers of the pyroxenite contribution in the major-element compositions of oceanic basalts: Review of the experimental constraints. Lithos, 160, pp.14-36.

Lambart, S., Baker, M.B. and Stolper, E.M., 2016. The role of pyroxenite in basalt genesis: Melt-PX, a melting parameterization for mantle pyroxenites between 0.9 and 5 GPa. Journal of Geophysical Research: Solid Earth, 121(8), pp.5708-5735.

Macris, C.A., Manning, C.E. and Young, E.D., 2015. Crystal chemical constraints on inter-mineral Fe isotope fractionation and implications for Fe isotope disequilibrium in San Carlos mantle xenoliths. Geochimica et Cosmochimica Acta, 154, pp.168-185.

Shorttle, O. and Maclennan, J., 2011. Compositional trends of Icelandic basalts: Implications for short–length scale lithological heterogeneity in mantle plumes. Geochemistry, Geophysics, Geosystems, 12(11).

Sossi, P.A. and O'Neill, H.S.C., 2017. The effect of bonding environment on iron isotope fractionation between minerals at high temperature. Geochimica et Cosmochimica Acta, 196, pp.121-143.

Vidito, C., Herzberg, C., Gazel, E., Geist, D. and Harpp, K., 2013. Lithological structure of the Galápagos Plume. Geochemistry, Geophysics, Geosystems, 14(10), pp.4214-4240.